Research Square

Preprints are preliminary reports that have not undergone peer review.
They should not be considered conclusive, used to inform clinical practice,
or referenced by the media as validated information.

Biosynthesis, Characterization, and Antimicrobial Activity of Gold Nanoparticles Using Chitosan Isolated From Portunus Sanguinolentus Shells

Dr. B. Sangeetha

sangigopi16@gmail.com

Dr. Ambedhkar arts and science college

Research Article

Keywords: Chitosan AuNPs, Gold nanoparticles, Portunus sanguinolentus, Biosynthesis, Antimicrobial activity, Characterization

Posted Date: November 10th, 2026

DOI: https://doi.org/10.21203/rs.3.rs-11221162/v1

License: This work is licensed under a Creative Commons Attribution 4.0 International License.
Read Full License

Additional Declarations: No competing interests reported.

BIOSYNTHESIS, CHARACTERIZATION, AND ANTIMICROBIAL ACTIVITY OF GOLD NANOPARTICLES USING CHITOSAN ISOLATED FROM *Portunus sanguinolentus* SHELLS

B. Sangeetha[a, *],

[a]Department of Zoology, Dr. Ambedkar government arts college, Chennai-39, Tamilnadu, India.

Corresponding author(s): sangigopi16@gmail.com (B. Sangeetha*)

ABSTRACT

Marine bio-nanotechnology has emerged as a promising field for developing eco-friendly nanomaterials with biomedical applications. This study reports the biosynthesis, characterization, and antimicrobial evaluation of chitosan-gold nanoparticles (CHS-AuNPs) using chitosan extracted from the exoskeleton of *Portunus sanguinolentus* (three-spot swimming crab) . Chitosan was successfully isolated from crab shell waste through sequential demineralization, deproteinization, decolorization, and deacetylation processes. The Chitosan-mediated AuNPs were characterized using UV-Visible spectroscopy, FT-IR, XRD, SEM-EDX, HR-TEM with SAED, DLS, and AFM techniques. UV-Vis spectroscopy revealed a characteristic surface plasmon resonance band at 529 nm, confirming the formation of gold nanoparticles. FT-IR analysis indicated the involvement of hydroxyl and amine groups in the reduction and stabilization of nanoparticles. XRD patterns confirmed the face-centered cubic crystalline structure of metallic gold, with Bragg reflections from the (111), (200), and (220) planes. SEM and HR-TEM images revealed predominantly spherical, polydisperse nanoparticles with sizes ranging from 8–10 nm (AFM) to 51.43 nm (DLS hydrodynamic diameter) . EDAX analysis confirmed the elemental composition with a strong gold signal. The antimicrobial activity of CHS-AuNPs was evaluated against six bacterial strains (*E. coli*, *Enterobacter*, *P. aeruginosa*, *K. pneumonia*e, S. aureus, and *E. faecalis*) and four fungal strains (*A. niger*, *Penicillium*, *Rhizopus*, and *A. flavus*) using the agar well diffusion method. The Chitosan-mediated AuNPs exhibited significant dose-dependent antibacterial activity, with the maximum zone of inhibition against S. aureus (22 ± 0.77 mm) and *P. aeruginosa* (22 ± 1.47 mm) at 40 µg/mL. Antifungal activity was highest against *Penicillium* (15 ± 0.57 mm) at the same concentration. The Chitosan-mediated AuNPs demonstrated superior

antimicrobial efficacy compared to chitosan alone, highlighting their potential as promising therapeutic agents in biomedical applications, particularly in drug delivery and infection control.

Keywords: Chitosan AuNPs, Gold nanoparticles, *Portunus sanguinolentus*, Biosynthesis, Antimicrobial activity, Characterization

1. Introduction

Marine bio-nanotechnology represents an emerging interdisciplinary field with immense potential for sustainable nanomaterial development. The marine environment harbors diverse micro- and macroorganisms, making it an ideal source for bio-nanotechnological exploration (Dhillon *et al*., 2011) . A key component of nanotechnology research is the development of a reliable, environmentally acceptable process for producing gold nanoparticles (AuNPs) (Manivasagan *et al*., 2016) . Nanoparticles with sizes below 100 nm exhibit novel or enhanced physicochemical properties compared to their bulk counterparts in terms of parameters including size, distribution, and form (Murugan *et al*., 2017) . The ability to control the size of NPs is highly desirable for most nanotechnology applications (Affes *et al*., 2020) . (Bahrami *et al*., 2014) NPs offer a wide variety of potential applications in catalysis, optical, photo-electrochemical, and antibacterial activities, as well as biomedicine and health care, due to their unique properties (Chen *et al*., 2020) . Different physicochemical techniques may be used to make NPs; however, these processes are highly reactive and pose significant environmental risks. Biomimetic techniques offer the benefit of employing nontoxic chemicals and ecologically benign solvents, as opposed to physicochemical approaches (Kalaivani *et al*., 2020, Begum *et al*., 2021, Emam *et al*., 2021, and Hajji *et al*., 2021) . Deacetylated chitin, also referred to as chitosan (CHS), is a naturally occurring polycationic linear polysaccharide produced when chitin is partially deacetylated (Begum *et al*., 2021) . Fig. 1 represents the chemical structure shift of chitin to chitosan by the action of the enzyme chitin deacetylase. Chitin is the second most prevalent natural polysaccharide after cellulose and is a structural component of the exoskeletons of insects and crustaceans (primarily prawns and crabs), as well as fungal cell walls. Chitin research was limited until the 1980s due to its complex structure, difficulty of extraction, and insolubility in aqueous solution. N-Acetyl-D-glucosamine and (1-4)-linked D-glucosamine are randomly distributed throughout the polymer that makes up chitosan. Since most polysaccharides are neutral or negatively charged in acidic environments, chitosan's cationic nature is somewhat unique. With other negatively charged synthetic or natural polymers, it can

form electrostatic complexes or multilayer structures (Novais *et al*., 2021; Salomatina *et al*., 2021)
.

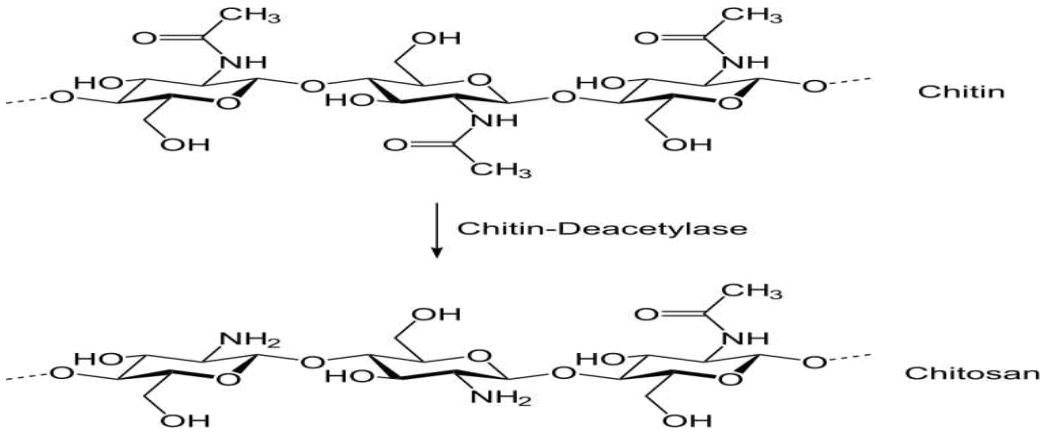


Fig. 1. Representation of the chemical structure of Chitin and chitosan.

Chitosan is widely recognized for its nontoxicity and great biocompatibility. Stabilizers, such as Chitosan, can help modify the surface's physical absorption, specific recognition, and electrostatic interactions during the formation of NPs, which is critical for assessing the potential therapeutic use of metal NPs (Novais *et al*., 2021) . Chitosan was utilized in the production of gold nanoparticles as a stabilizer and reducing agent. The concentration of Chitosan influences the size and stability of NPs (Salomatina *et al*., 2021) . Chitosan interacts with anionic Gold (III) chloride hydrate ions, producing electrostatic attraction between metal anions and protonated amine groups (Sivanesan *et al*., 2021) . The biosynthesis of metallic NPs is gaining prominence owing to its eco-friendliness and low cost. Chemical methods, on the other hand, are associated with biological hazards and environmental impact (Sun *et al*., 2021) . Metallic NPs derived from biological agents such as microorganisms, fauna, and flora are extremely stable (Lv *et al*., 2021) . Many studies have investigated the uses of gold nanoparticles (AuNPs) in the health sciences; moreover, predicted NP sizes derived from spectroscopic measurements have been examined. Furthermore, this study will help explore the medicinal benefits of Chitosan, paving the way for the therapeutic application of *Portunus sanguinolentus* crab shells. The particle size, shape, and nanocrystallinity of Chitosan AuNPs were investigated.

The Kasimedu fish landing center, Chennai, served as the source of raw crab shell material. Marine crustacean shell waste generated at such landing centers is an abundant, low-cost, and

renewable source of chitin and chitosan, and its valorization helps reduce coastal pollution (Santos *et al*., 2020) . The three-spot swimming crab, *Portunus sanguinolentus*, collected from this site has been recognized as a suitable species for chitosan extraction owing to the high crustacean biomass available in the region (Pradhan *et al*., 2024) . The specimen shown belongs to the family Portunidae and was authenticated as *Portunus sanguinolentus* (three-spot swimming crab) . The exoskeleton of this species has previously been exploited for chitosan recovery through sequential deproteinization, demineralization, depigmentation, and deacetylation (Tanasale *et al*., 2012) . Recent studies have also demonstrated the physico-chemical and biological potential of chitosan derived from *Portunus sanguinolentus* shells, validating its use as a biopolymer source for nanomaterial synthesis (Pradhan *et al*., 2024) . The roughness and wettability of Ti were consistently enhanced as the thickness of G increased. However, other parameters, such as cell survival and corrosion resistance, needed to be optimized because they decreased as G mesolayer thickness increased. However, the application of G and CHAP PCL coatings in this work resulted in considerable enhancements in all examined physical and chemical properties of Ti.

The potential of this multilayer design for the development of biomaterials for orthopedic implants and tissue engineering is clearly evident (Fathi *et al*., 2021) . A study was conducted to analyze the electrical properties of polyvinylidene fluoride (PVDF)/polyvinyl chloride (PVC) composites after exposure to gold nanoparticles (AuNPs) via a one-way laser ablation technique. Nanocomposites of AuNPs PVDF/PVC were produced in films using the conventional casting procedure. The electrical conductivity of films made from AuNPs PVDF/PVC was also investigated (Tommalieh *et al*., 2020) . A film made from poly (vinyl alcohol)/chitosan (PVA/CS) embedded with vanadium oxide nanoparticles (V2O5 NPs) was created. This film is both ecologically friendly and cost-effective. The objective of using V2O5 nanoparticles is to enhance the antibacterial properties of the resulting PVA/CS film. The structural, optical, and morphological characteristics, as well as thermogravimetric analysis, of the PVA/CS/V2O5 NPs nanocomposite films were thoroughly investigated to determine the impact of two different concentrations of added V2O5 NPs (Menazea *et al*., 2021) . The development of novel biomaterial compositions suitable for the regeneration of hard tissues is crucial and desirable for enhancing global quality of life. They employed a laser deposition (PLD) approach; hydroxyapatite (HAP) was sputtered on a donose substrate. During interexposure intervals, analysis of surface morphology indicated that alumina grains had diameters of approximately 1.3–2.94 μm, and a high

degree of porosity was observed (El-Kader *et al*., 2021) . The synthesis of core-shell AuSe nanoparticles (AuSe NPs) and their incorporation into a solution of polymeric nanofibrous cellulose acetate (CA)/polyvinylidene fluoride (PVDF) was achieved using a pulsed laser ablation system. The resulting solution was then electrospun. The nanofibrous scaffolds can be modified to achieve a novel design for the treatment and regeneration of injured tissues (Aldalbahi *et al*., 2020) . Zinc oxide (ZnO) was synthesized from Hibiscus rosa-sinensis extract using an environmentally friendly preparation approach. Suggesting eco-friendly composites devoid of toxic compounds for biological purposes (El-Kader *et al*., 2021) .

Different proportions of bismuth (III) oxide nanoparticles (Bi2O3 NPs) dispersed in Chitosan/Poly (Vinyl Pyrrolidone) are used in electronic devices and for antibacterial applications. Nanocomposite films consisting of Chitosan, PVP, and Bi2O3 have been produced by laser ablation. The incorporation of Chitosan/PVP/Bi2O3 NPs results in significant enhancements in both electrical conductivity and antibacterial efficiency. Therefore, it is highly recommended to investigate these compositions further for potential applications in electrical and biomedical fields, such as wound dressing and infection control (Elabbasy *et al*., 2021) . Graphene oxide nanoparticles (GONPs) were synthesized via laser ablation and incorporated into a new Chitosan-Poly (Vinyl Pyrrolidone) (PVP) blend for microbial applications. After graphene oxide was added, the structural and optical characteristics of pure Chitosan-PVP were examined. Based on further research, the resulting compositions may be recommended for use in microbiological applications (Mogbel *et al*., 2021) . Solution casting was used to create nanocomposite films made of Poly Vinyl Pyrrolidone/Chitosan (PVP/Chitosan) and filled with vanadium pentoxide nanoparticles (V2O5 NPs) . Using the one-potential laser ablation approach, vanadium pentoxide nanoparticles were scattered directly into the PVP/Chitosan combination.

The manufactured PVP/Chitosan/V2O5 NP films could be used in electrical and optoelectronic applications (Menazea *et al*., 2021) . Selenium nanoparticles (Se NPs) were manufactured using the laser ablation procedure. PEO/Cs (70% PEO/30% Cs) were doped with Se NPs at different ablation times. XRD measurements showed a decrease in crystallinity in the produced films. Electrical conductivity studies demonstrated that increasing the concentration of selenium nanoparticles in PEO/Cs increased the dielectric performance of the films. Electrical relaxation dynamics were investigated in the presence of a dielectric (Alzahrani *et al*., 2022) . In

the present work, we investigated the biosynthesis of Chitosan-containing gold nanoparticles (CHS-AuNPs), derived from the crab shell of *Portunus sanguinolentus*. The formation of CHS-AuNPs has been confirmed by UV-Visible, FT-IR, XRD, SEM with EDAX, TEM, DLS, and AFM. The Chitosan-mediated AuNPs were also screened for their antimicrobial activities. 2. Materials and Methods

2.1 Chemicals and reagents

The required chemicals were purchased from the following source: Gold (III) chloride hydrate from Sigma-Aldrich. Distilled water with a resistivity of 6.4-6.5 and a pH of 6.5 was used for all the experiments. All analytical-grade chemicals were purchased from Merck, Bangalore, India. Culture media were purchased from HiMedia, Mumbai, India.

2.2 Collection of crab shells



Crab shells were collected from the fish landing center at Kasimedu, Tamil Nadu. Fig. 2 shows the specific location marking the study area, Kasimedu fish landing center.

Fig. 2: Study area showing the Kasimedu fish landing center

2.3 Identification of crab

Species *Portunus sanguinolentus* was collected from Kasimedu fish landing center (13° 7′ 31.98″ N, 80° 17′ 51.52″ E), Chennai, Tamil Nadu, India. Dr. C.P. Balasubramanian, Principal Scientist, Crustacean Culture Division, Central Institute of Brackish Water Aquaculture, Chennai, Tamil Nadu, authenticated the crab's identification as *Portunus sanguinolentus*, a member of the family Portunidae. Fig. 3 showcases the anterior region of the crab shell, *Portunus sanguinolentus.*



Fig. 3: *Portunus sanguinolentus* anterior region of the crab shell

2.4 Preparation of Crab Shell

Shell Powder Chitin and chitosan were isolated using standard chemical methods including demineralization, deproteinization, decoloration, and deacetylation (Fig. 3) . The detailed illustration is as follows: The exoskeletons of 30 g crabs were placed in a 250 mL beaker and treated with sodium hydroxide (4% v/v) before being heated for 1 hour to break down proteins and carbohydrates and isolate crude chitosan. The sample was then allowed to cool at room temperature for 30 minutes. 2.5 Chitin extraction 2.5.1 Demineralization The removal of minerals, primarily calcium carbonate, is known as demineralization. Demineralization involves the removal of minerals, primarily calcium carbonate, through the release of carbon dioxide and formation of water-soluble calcium salts, as shown in the following equation: $2HCl + CaCO_3 \rightarrow CaCl_2 + H_2O + CO_2\uparrow$. The resulting chitin solid phase is then filtered and washed with deionized water to remove soluble salts.

$$2HCl + CaCO3 \rightarrow CaCl2 + H2O + CO2 \uparrow$$

For demineralization, two molecules of HCl are required to convert one calcium carbonate molecule into a calcium chloride molecule. Acid intake needs to be at least as big as the stoichiometric amount of minerals for a full reaction to occur. Due to the heterogeneity of the material, it is difficult to extract all minerals; hence, a larger volume or more concentrated acid solution is employed. Acidimetric titration can be used to monitor demineralization because the evolution of pH towards neutrality corresponds to acid consumption, while the persistence of acidity in the medium signals the end of the reaction. Demineralization treatments can be administered using a variety of concentrations (up to 10% w/v) at room temperature over the

course of an hour. After one hour, the processed shells were washed thoroughly in running tap water until they reached neutral pH.

2.5. Chitin extraction

2.5.1 Deproteinization

The chemical interactions between chitin and proteins must be disrupted during deproteinization, a challenging process. This is accomplished heterogeneously using chemicals that completely remove the protein and depolymerize the biopolymer. The reagents for deproteinization include NaOH, Na2CO3, NaHCO3, KOH, and K2CO3. Deproteinization was performed using 5% (w/v) NaOH in a 1:10 (shell:NaOH) ratio at 100°C for 1 hour in a water bath. After one hour, it is cooled to room temperature and filtered; the washing in running water continues, and the pH is then checked to ensure it is neutral. The final product is called chitin.

2.5.2 Decolouration

The identical samples were collected in a glass beaker containing potassium permanganate (KMnO4) and then kept in water for 3 h. Afterward, the samples were washed 5 to 7 times with water until the pH reached neutral. We obtained chitin from different samples in the product name after washing the aforementioned three methods.

2.6 Deacetylation of Chitin to Chitosan

Deacetylation is one of the primary processes that occur on chitin. Although in theory amides might be deacetylated under acidic or basic conditions, using acid hydrolysis is not an option because chitin's glycosidic linkages are resistant to acid hydrolysis. Since the acetamido group is sensitive to alkaline hydrolysis, deacetylation requires harsh conditions. Deacetylation is done using a OH (1% w/v) NaOH solution and maintained at 60 °C for 1 hour, then cooled to room temperature. Then, finally, check that the pH is neutral.



Fig. 4 Sequential steps for the isolation of chitosan

The isolation procedure followed the classic chemical extraction route: deproteinization, demineralization, decoloration ($KMnO_4$) and finally deacetylation to convert chitin into chitosan (Santos *et al*., 2020) . Fig. 4 shows the sequential steps for chitosan isolation. In this process, mineral removal is achieved by acid treatment, while alkaline conditions depolymerize proteins and cleave acetyl groups; the choice of reagent concentration, temperature, and duration critically governs the yield and degree of deacetylation of the recovered chitosan (Younes & Rinaudo, 2015) . Optimization studies on crustacean shell waste similarly report acid demineralization and alkaline deproteinization/deacetylation as the standard conditions for high-quality chitosan production (Amoo *et al*., 2019) .

2.7 Synthesis of CHS-AuNPs

The technique used by Villa-Garcia *et al*. for chitosan-mediated AuNPs was followed (2021) . In a 400 mL beaker, 10 g of chitosan powder was combined with 100 mL distilled water to make a chitosan aqueous extract for the reduction of Au+ ions to Au0. The mixture was then heated for 10 minutes at 34°C in a 10,000-rpm magnetic stirrer. The resulting chitosan aqueous extract was filtered using Whatman No. 1 filter paper to achieve a pure extract in a typical experiment. In a 1 mM aqueous Gold (III) chloride hydrate solution, 5 mL of chitosan aqueous extract was added (45 mL total) . Excitation of Surface Plasmon vibration caused the color shift, as evidenced by the decrease of Au+ ions to Au0. AuNPs were spun at 15,000 rpm for 30 minutes after the reaction was completed. The supernatant was discarded, and the fine sediment pellet was

centrifuged once more in distilled water to remove any biomaterials that might interfere with Au+ binding to biomass or with AuNP formation.

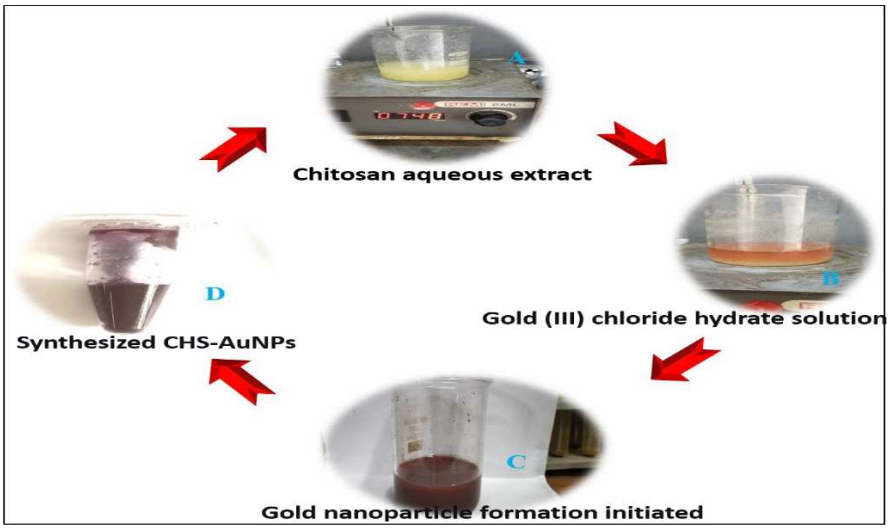


Fig. 5: A- Chitosan aqueous extract (bright clear white color), B- 1 mM aqueous Gold (III) chloride hydrate solution (light yellowish color), C-elevation of light pink denotes the synthesis of Au+, and D- indicates the dark pink coloured AuNPs.

The stepwise color transition from bright white (chitosan extract) through light yellow (gold chloride), light pink, and dark pink provides visual evidence of gold nanoparticle formation. Fig. 5 shows the overall process of gold nanoparticle synthesis from chitosan aqueous extract, highlighting the color changes. This color change arises from the excitation of surface plasmon vibrations as Au^{3+} is reduced to Au^{0} (Mohan *et al*., 2019). Chitosan acts simultaneously as the reducing and stabilizing agent, capping the newly formed nanoparticles, and chitosan-capped AuNPs characteristically display this pink-to-red coloration associated with their surface plasmon resonance (Cazacu *et al*., 2022; Fathil *et al*., 2022).

2.8 Characterization of chitosan Gold nanoparticles (AuNPs)

Shape, size, surface area, and dispersity are characteristics of the Chitosan-mediated AuNPs of aqueous extract of chitosan. All characterization approaches were carried out in accordance with accepted procedures. Ultraviolet-Visible (UV-Vis) spectroscopy, Fourier transform infra-red (FT-IR) spectroscopy, X-ray diffraction (XRD), Scanning Electron Microscope (SEM) with Energy-dispersive X-ray diffraction spectroscopy (EDX) High-Resolution, Transmission Electron Microscopy (HR-TEM) with Selected Area Electron Diffraction (SAED), Dynamic Light Scattering (DLS), Atomic Force Microscopy (AFM).

2.9 Antimicrobial Sensitivity Assay

Antibacterial and antifungal sensitivity assays were carried out according to the standard methods of Vijilvania *et al*. (2020)

2.9.1 Preparation of Mueller-Hinton Agar (MHA)

Beaf extract	300g
Cas amino acid	17.5gms
Starch	15gms
Agar	17gms
Ph	7.4gms

Muller-Hinton agar (38 g) was dissolved in 1000 mL of double-distilled water and heated until completely dissolved. The medium was then autoclaved at 121 °C and 15 psi for 15 minutes. 2.9.2 Antibacterial activity (Agar Well Diffusion) The chitosan aqueous extract and its AuNPs were screened for antibacterial activity against the above-mentioned organisms given in Table 2, selected in the present study. The prepared Mueller-Hinton agar medium was poured onto the sterile Petri plates and allowed to solidify. The test organisms were inoculated in the Nutrient Broth (NB) and incubated overnight at 37°C. A lawn culture was made on Mueller-Hinton agar plates using the inoculum and allowed to dry for 10 minutes. Wells (diameter 6mm) were punched on the sterile plates using a cork borer. The aqueous extract of chitosan and Chitosan-mediated AuNPs (10µg, 20µg, 30µg and 40µg/ml) were loaded into the various concentration wells in agar plates. Amikacin was used as the standard, and the plates were incubated at 37 °C for 24 hours. The antibacterial activity was measured in mm (i.e., the formation of the zone of inhibition around the well.

2.10 Antifungal activity (Agar Well Diffusion)

2.10.1 Preparation of Sabouraud's Dextrose Agar (SDA)

Ingredients	**Gram / 1 Liter**
Dextrose	40 g

Mixtures of peptic digest of animal Tissue	5 g
Distilled/ Purified water	1000 ml
Agar	15 g
pH after sterilization (at 25°C)	5.6 - 0.2

Antifungal activity was tested against the fungal strains selected for the study by the agar well diffusion method. Sabouraud's dextrose agar was prepared and sterilized in an autoclave at 121 °C and 15 psi for 15 minutes. The prepared medium was poured onto the sterile Petri plates and allowed to solidify. The inoculum was prepared and adjusted to the McFarland 0.5 standard. Lawn culture was prepared on sterile agar plates, then allowed to dry for 10 minutes, and wells (diameter 6mm) were punched using a cork borer. The aqueous extract of chitosan and Chitosan-mediated AuNPs (10µg, 20µg, 30µg and 40µg/ml) were loaded into the various concentration wells in agar plates. Fluconazole was used as a positive control, and the plates were incubated at room temperature for 48-72 hours. The antifungal activity was measured as mm, i.e., formation of the zone of inhibition around the well.

RESULTS AND DISCUSSION

3.1 UV-VIS Spectral analysis

Due to electron excitation in chitosan, which reduces Au3+ to Au0, AuNPs were produced using chitosan aqueous extract for 20 minutes, as it contains fewer active chemicals under room conditions. The color shift from yellow to pink at a wavelength of 510–580 nm indicates the production of AuNPs. After 7 days, the stability observations revealed a greater max shift and a substantial drop in absorbance, indicating agglomeration. At ambient temperature, oxidation of functional active chemicals in the aqueous extract may yield keto forms, which act as a reducing agent for Au3+ to Au0. As a result, we hypothesized that the Chitosan aqueous extract employed in this work may not only decrease gold ions but also act as an effective capping agent, stabilizing AuNPs via electrostatic and/or steric repulsion at 529 nm. Fig. 6 (a) and (b) show UV spectral analysis of chitosan and chitosan–based AuNPs.

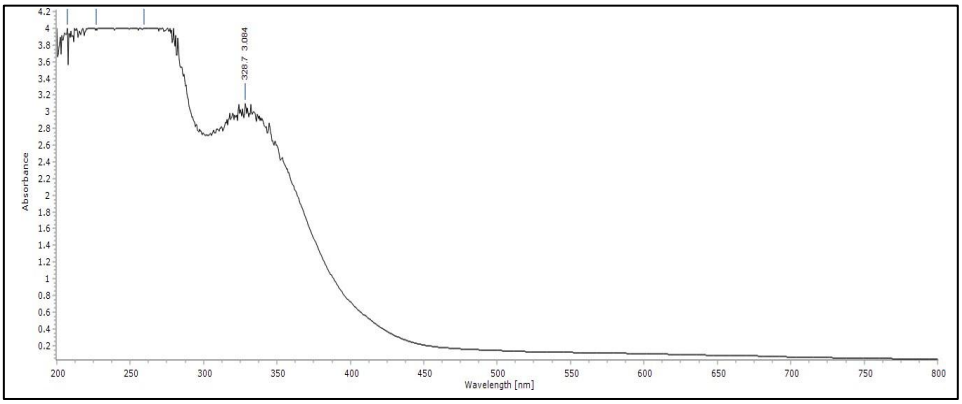


Fig. 6 (a): UV spectral analysis of Chitosan

The UV spectrum of the aqueous chitosan extract showed characteristic absorption in the UV region. UV absorption measurements are routinely used to evaluate the spectral quality of extracted chitosan, since the polymer's absorption profile reflects its molecular structure and purity (Hao *et al*., 2021). In the present study, this spectrum served as the baseline against which the appearance of the AuNP-specific surface plasmon band could be distinguished.

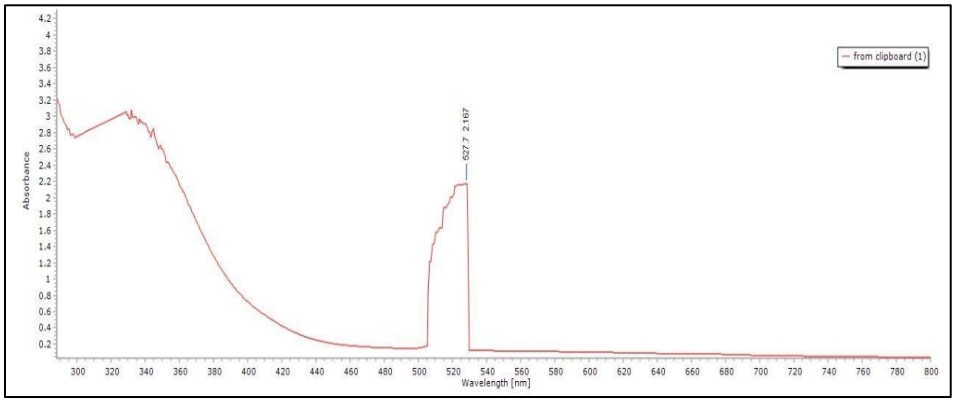


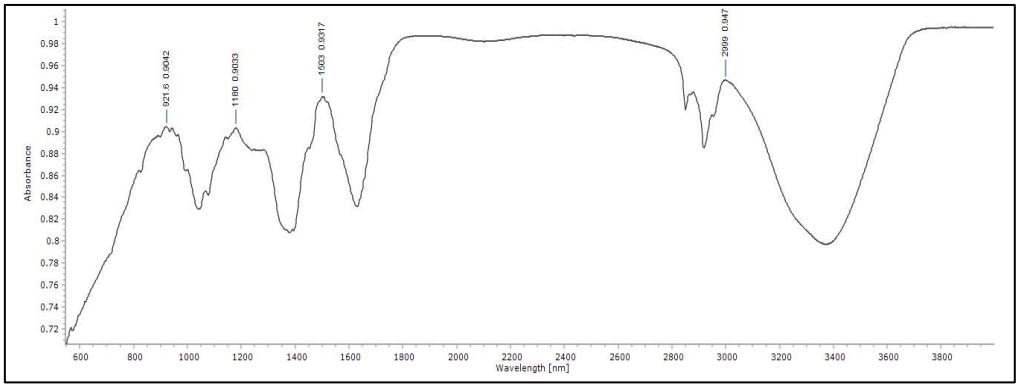
Fig. 6 (b)UV Spectrum of Chitosan-based AuNPs

The spectrum of the Chitosan-mediated AuNPs exhibited the characteristic localized surface plasmon resonance band centered at 529 nm, which arises from the collective oscillation of conduction electrons induced by the incident electromagnetic field (Mohan *et al*., 2019). Comparable λmax values (526–540 nm) have been reported for chitosan-capped AuNPs, with the peak position shifting with particle size, shape, and concentration (Mohan *et al*., 2019). Chitosan-stabilized AuNPs synthesized with other biological reducing agents likewise show SPR

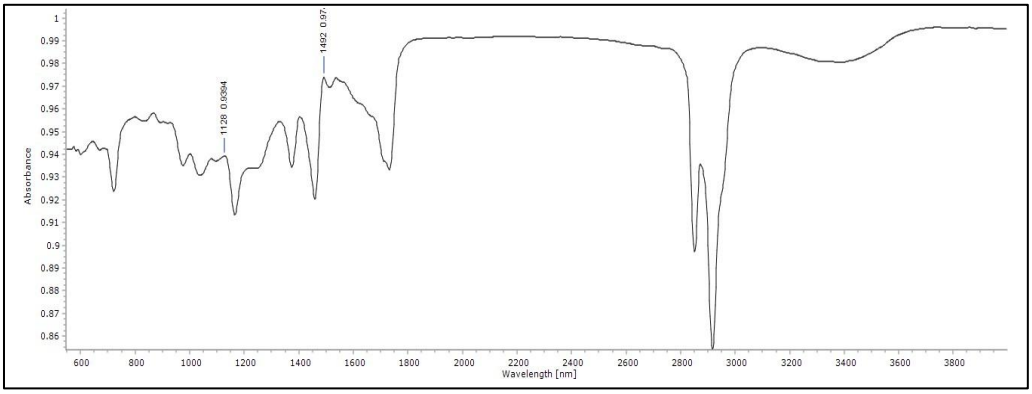
bands around 533 nm, corroborating the formation of stable, nanosized AuNPs in the present work (Katas *et al*., 2018).

3.2 FT-IR spectral analysis

To determine the potential functional groups of the bioactive compounds involved in the biosynthesis process, FT-IR scans over the 600-3800 cm-1 wavenumber range were conducted. The FTIR spectra of chitosan aqueous extract and synthesized nanoparticles showed strong and broad bands at 921.6 cm-1, 1180 cm-1, 1603 cm-1 and 2999 cm-1, corresponding to stretching vibrations of the surface hydroxyl group (-OH) and can also be attributed to N-H stretching of the C-OH stretch (strong) and -C-H aldehydic (variable) in Chitosan aqueous extract. The present study's -CH2band (medium) and -C-OH (strong) molecular stretching is thought to be the cause of the AuNPs' dramatic peak at 1128 and 1492 cm-1. Fig. 7 (a) and (b) show FT-IR spectral images of chitosan aqueous extract and Chitosan AuNPs.



A



B

Fig. 7: FT-IR spectral image A- Chitosan aqueous extract and B-Chitosan AuNPs X-ray Powder Diffraction (XRD)

The FT-IR spectrum of chitosan exhibited the characteristic polysaccharide bands: the broad O–H/N–H stretching region, C–H stretching vibrations, amide I (C=O) and amide II (N–H) absorptions, and the glycosidic C–O–C fingerprint bands between 1150 and 900 cm^{-1} (Corazzari *et al*., 2014) . These assignments are consistent with standard literature values for chitosan, in which the ~3400 cm^{-1} (–OH), ~1620–1655 cm^{-1} (amide I), and ~1530–1580 cm^{-1} (amide II/N–H bending) bands are diagnostic (Takara *et al*., 2015) . In the AuNP spectrum, the shifts of the peaks at 1128 and 1492 cm^{-1} indicate the involvement of –C–OH and $–CH_2$ groups in the reduction and capping of gold, confirming the interaction between chitosan and the nanoparticle surface.

3.3 XRD

XRD was used to validate crystallinity and determine the material's structural phase. XRD shows the diffraction pattern at Cu K-alpha with the wavelength of the light source (=0.154056 Angstrom) . For face-centered cubic (FCC) metallic gold, Bragg reflections were detected at 2θ = 38.17°, 43.62,° and 64.60°, corresponding to the lattice planes (111), (200), and (220) (JCPDS 03-1174) . The intensity ratio between the planes verifies the article's preferred orientation in the (111) plane, which is typical of the FCC crystalline structure. A number of unassigned peaks were detected in addition to these reflection peaks, which can be attributed to salt residues and bio-organic phases on the surface of the AuNPs. The crystal structure of AuNPs was shown in the FCC lattice structure as an atom at each cube corner and an atom in the center of each cube face. It is a densely packed plane in which atoms are supposed to contact along face diagonals on each face of the cube, and each edge of the cube is 4.07 in length.

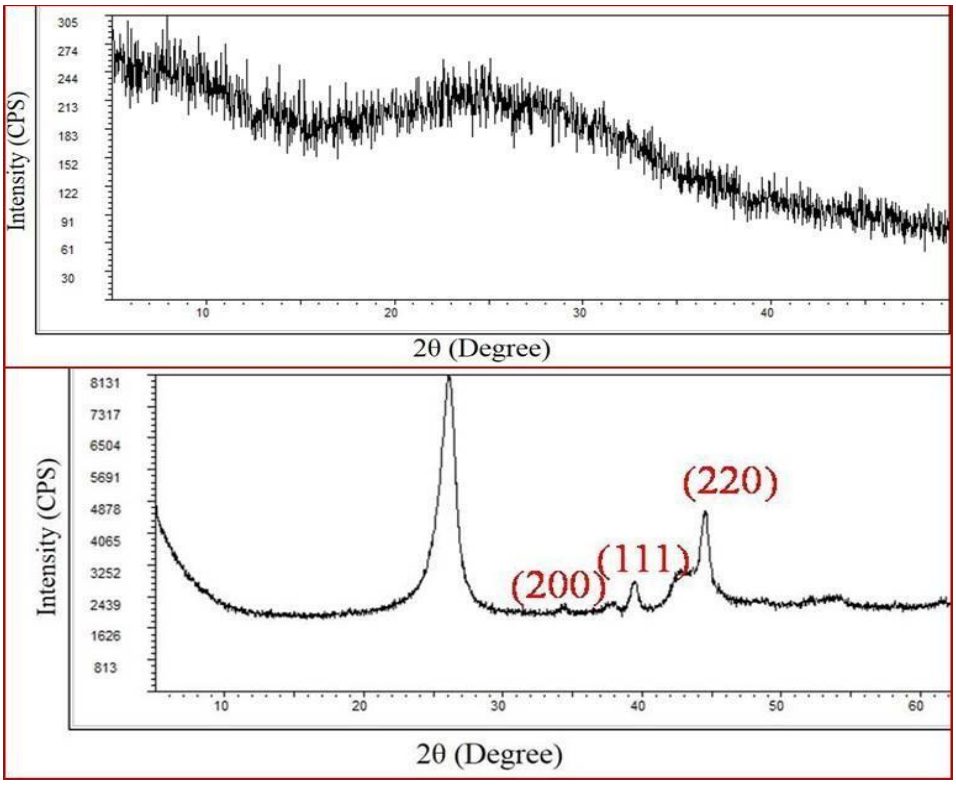


Fig. 8: XRD spectral image A- Chitosan aqueous extract and B-Chitosan AuNPs SEM

The diffraction pattern of the AuNPs showed Bragg reflections at 2θ = 38.17°, 43.62°, and 64.60°, corresponding to the (111), (200), and (220) planes of the face-centered cubic lattice of metallic gold (JCPDS 03-1174) . The intense (111) reflection indicates preferential crystalline growth along this plane, which is typical of FCC gold (Boruah *et al*., 2021) . Comparable peaks at 38.1°, 44.3°, 64.5°, and 77.4° have been widely reported for biosynthesized and chemically Chitosan-mediated AuNPs, confirming the highly crystalline nature of the particles (Wu & Chen, 2010) . The additional unassigned peaks are attributable to salt residues and bio-organic phases on the particle surface. Fig.8 confirms the chitosan and crystalline nature of chitosan-based AuNP's.

3.4 SEM

SEM micrograph of the Chitosan-mediated AuNPs from chitosan aqueous extract shows the presence of spherical polydispersive nanoparticles with particle size ranging from below 100 nm in size of varying shapes such as spherical and square. While, SEM image of chitosan also showed polydispersive nature and the sample contained mostly aggregates

of amorphously shaped particles. The nanoparticles were not in direct contact even within the aggregates, indicating stabilization of the AuNPs by a capping agent.

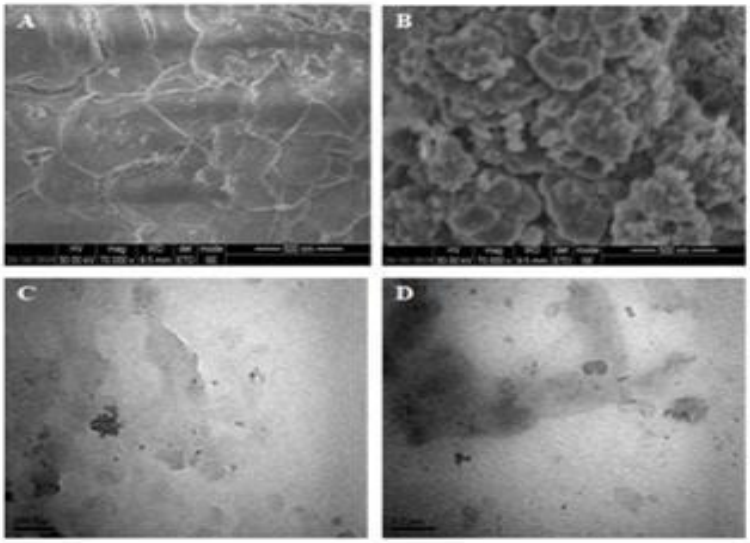


Fig. 9 SEM images of Chitosan

The SEM micrographs of chitosan showed a polydisperse, aggregated, and largely amorphous morphology, typical of chitosan powder and films, in which micro- and nano-sized pores are frequently observed (Choudhary *et al*., 2017) . SEM is the standard tool for morphological characterization of biopolymer-based nanomaterials, providing direct evidence of surface texture and particle organization at the micrometer-to-nanometre scale (Joudeh & Linke, 2022) . Fig. 9 represent the SEM image of chitosan.

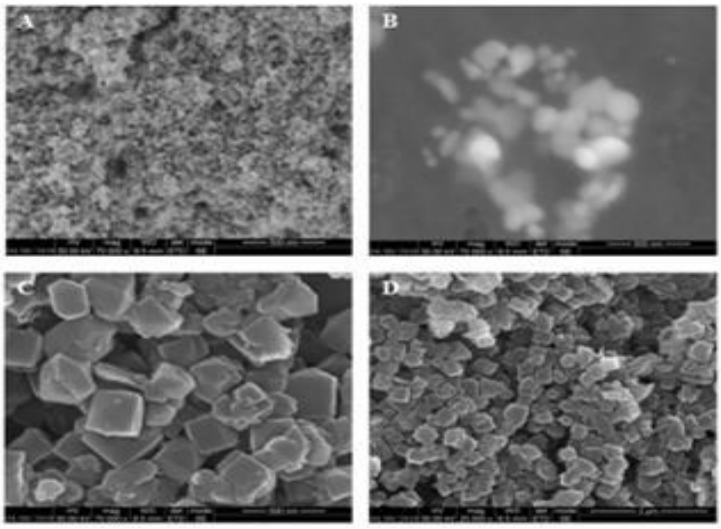


Fig. 10 SEM images showing different sizes and shapes of Chitosan-mediated AuNPs

The SEM images revealed predominantly spherical, polydisperse nanoparticles with sizes below 100 nm and mixed spherical/square outlines. Green-synthesized gold nanoparticles typically exhibit a spherical morphology regardless of the biological reducing agent used, with diameters commonly reported between 50 and 80 nm (Koliyote & Shaji, 2023). The observation that particles remained separated even within aggregates indicates stabilization by the chitosan capping layer, and the SEM size range is consistent with that inferred from TEM and DLS measurements (Boruah *et al*., 2021) . Fig.10 represent the SEM image showcasing different size and shapes of chitosan-mediated AuNPs.

3.5 EDAX

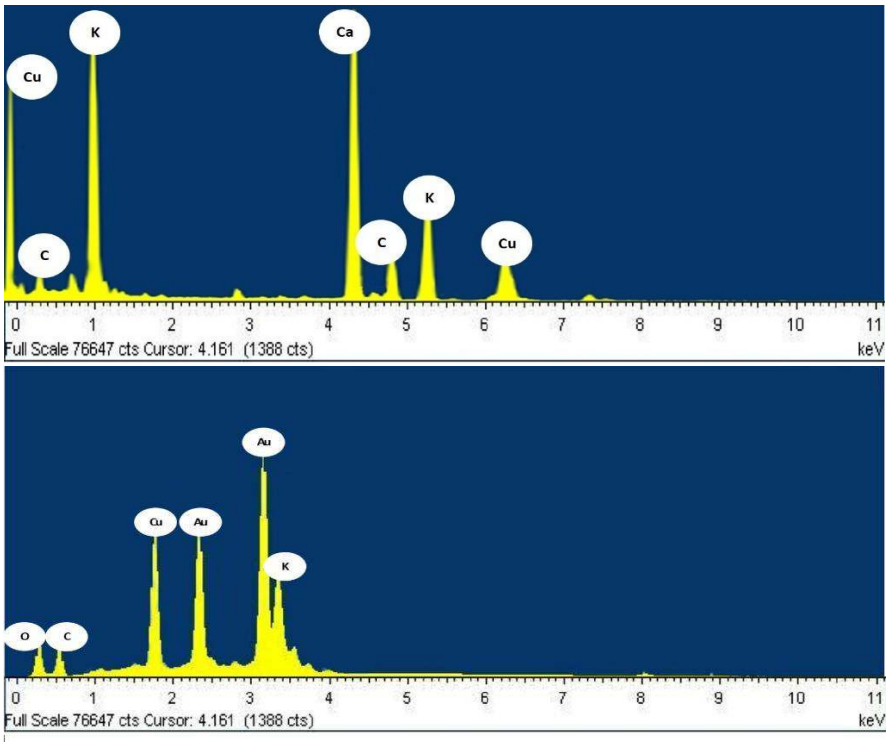


Fig. 11 (a) (b) EDAX images of chitosan and AuNPs

The EDAX spectrum of chitosan showed elemental peaks of C, K, and Ca, attributable to the organic polymeric matrix and residual biomineral constituents retained from the crab shell, together with a Cu signal arising from the copper grid used for sample mounting. Energy-dispersive X-ray analysis is routinely employed to confirm the elemental composition of biogenic samples, with carbon and oxygen signals reflecting the biomolecular capping layer (Joudeh & Linke, 2022; Nguyen *et al*., 2021).

The EDAX profile of the AuNPs displayed a strong characteristic gold signal, confirming the pure, crystalline metallic nature of the nanoparticles, along with weaker signals from O, C, Cu,

and K, originating from the bio-organic capping layer and the copper grid. Strong Au absorption peaks around 2.2–2.4 keV are well documented in metallic gold nanoparticles, with accompanying C and O signals attributed to biomolecules that stabilize the particles (Alhumaydhi *et al*., 2021; Nguyen *et al*., 2021) . EDAX image of chitosan showed elemental peaks of C, K, and Ca, indicating the presence of complex active compounds, and a Cu peak attributed to the sample coated on the copper grid. The elemental composition of AuNPs was characterized by EDAX. It shows a strong signal, indicating the pure, crystalline nature of AuNPs. Detection of weak signals from O, C, Cu, K, and Au were also recorded. Fig. 11 (a) and (b) showcase the EDAX images of chitosan and chitosan-based AuNPs.

3.6 Atomic Force Microscopy (AFM)

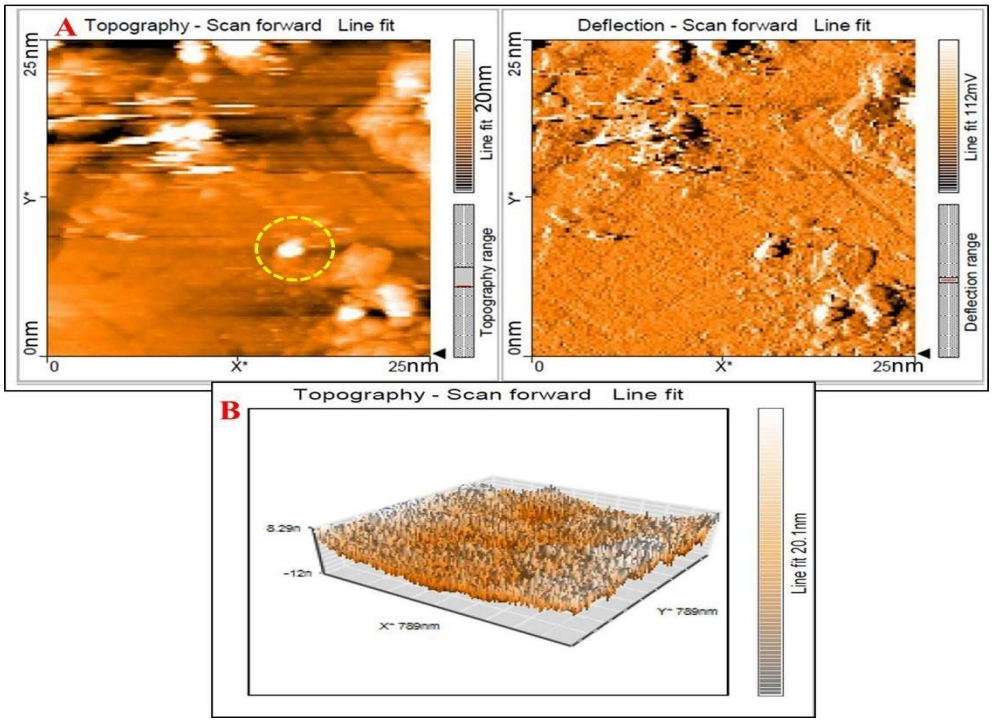


Fig. 12 synthesized chitosan-based gold nanoparticles

The 3D AFM topographs revealed a homogeneous distribution of the AuNPs and enabled particle sizing via granularity accumulation distribution analysis, yielding an average particle diameter of 8–10 nm. AFM provides both qualitative and quantitative information on size, morphology, and surface texture, and is widely used to generate 2D/3D images and size histograms of nanoparticles (Ghafoor *et al*., 2019) . Similar 3D AFM imaging has been applied to size AuNPs produced by green and physical methods, with the observed spherical geometry correlating well with TEM results (Mytlak, 2018). The AFM 3D images indicate a homogeneous distribution of gold nanoparticles, with no agglomeration observed. Fig. 12 shows the AFM images for 1 mM gold trichloride hydrate concentration, where the particle shape and size were indicated. Some

agglomeration was observed at 8nm and 10 nm with large nanoparticle diameters. AFM shows the Granularity Accumulation Distribution (GAD), which provides the particle-size distribution of gold nanoparticles. The average particle diameter of the synthesized gold nanoparticles is between 8 and 10 nm. Yellow-colored circles represent the ovoid-shaped gold nanoparticles. The large diameter could be due to particle sedimentation, resulting in decreased absorbance. The AFM analysis confirmed the nanosphere shapes of the gold nanoparticles, which correlate with the TEM image.

3.7 HR-TEM

The HR-TEM images presented in Fig. 13 show biosynthesized samples containing well-dispersed chitosan AuNPs with average sizes closer to the estimated values from the DLS study. While the aqueous extract of chitosan AuNPs formed is non-spherical, containing multiple facets, HR-TEM images revealed that the chitosan AuNPs are highly crystalline, with an occasional presence of twin boundaries.

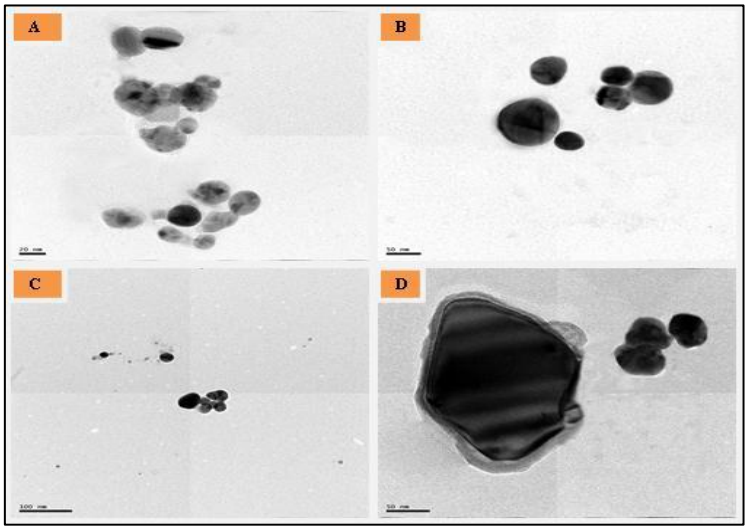


Fig. 13 HR-TEM image of Chitosan-mediated AuNPs

The HR-TEM micrographs showed well-dispersed AuNPs with multiple facets and occasional twin boundaries, indicating high crystallinity. High-resolution TEM directly reveals lattice features such as twin boundaries and polycrystalline domains in gold nanoparticles (Zhou *et al*., 2012) . TEM/HR-TEM offers substantially higher resolution than SEM for nanoscale morphological and structural analysis, making it the definitive technique for verifying nanoparticle size, shape, and crystallinity (Mourdikoudis *et al*., 2018) .

3.8 SAED

The crystallinity of AuNPs was assessed using XRD and SAED. Fig. 14 shows the SAED patterns of the chitosan-based AuNPs nanoparticles. The ring pattern in SAED further confirms that the AuNPs formed are crystalline in nature.

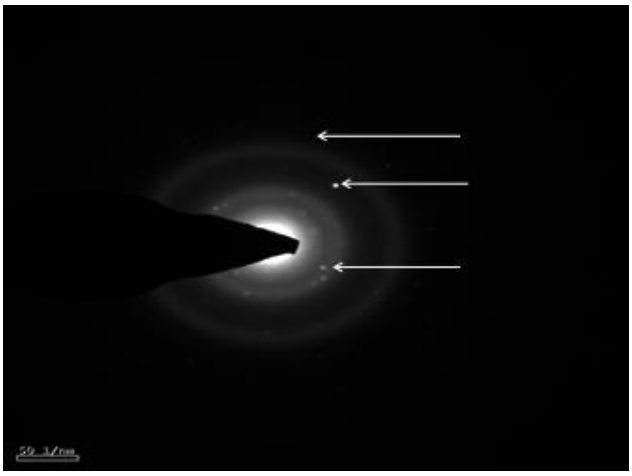


Fig. 14 SAED pattern corresponds to HR-TEM images of Chitosan-mediated AuNPs

The selected-area electron diffraction pattern displayed bright concentric rings corresponding to the (111), (200) and (220) planes of FCC gold, confirming the crystalline (polycrystalline) nature of the nanoparticles (Hans *et al*., 2023) . The ring ratios observed are characteristic of the FCC lattice of metallic gold and are consistent with the XRD results, jointly confirming the crystallinity of the CHS-AuNPs (Wu & Chen, 2010) .

3.9 Dynamic Light Scattering (DLS)

DLS showed a size-distribution-versus-intensity graph. The average size of CHS-AuNPs at a 1 µM concentration of Gold (III) chloride hydrate was 51.43 nm, and they were monodispersed. The small particle size observed by DLS is due to the encapsulation of bioorganic compounds acting as capping agents for AuNPs, whereas DLS of chitosan showed many large particles. This is due to its linear polysaccharide nature, as shown. While the formation of relatively large particle sizes in the chitosan samples can be associated with the presence of complex compounds, the DLS analysis of the samples indicates a clear, homogeneous size distribution for all the samples, which contrasts with their TEM images. Therefore, these samples were analyzed further using a transmission electron microscope.

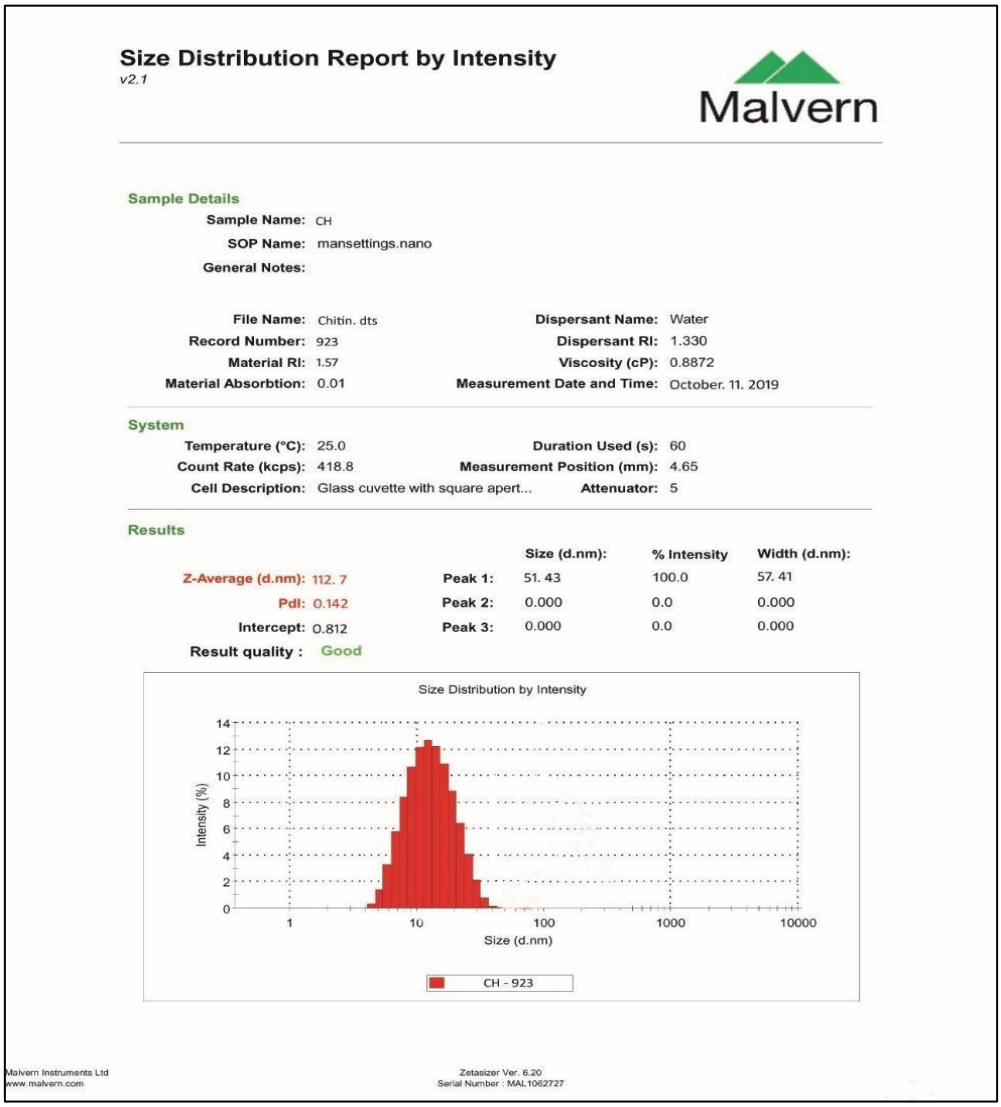


Fig. 15 (a) DLS analysis of chitosan aqueous

The DLS profile of the aqueous chitosan showed a broad size distribution dominated by large particles, consistent with the linear, high-molecular-weight polysaccharide nature of chitosan. DLS measures the hydrodynamic diameter, which for polymer-coated species includes the swollen polymer shell and is therefore reported as substantially larger than the true core size (Geertsen *et al*., 2018) ; DLS remains the standard technique for obtaining size and size-distribution information on colloidal suspensions (Zheng *et al*., 2016). Fig. 15 (a) and (b) showcases the DLS analysis of aqueous chitosan and chitosan-based AuNPs.

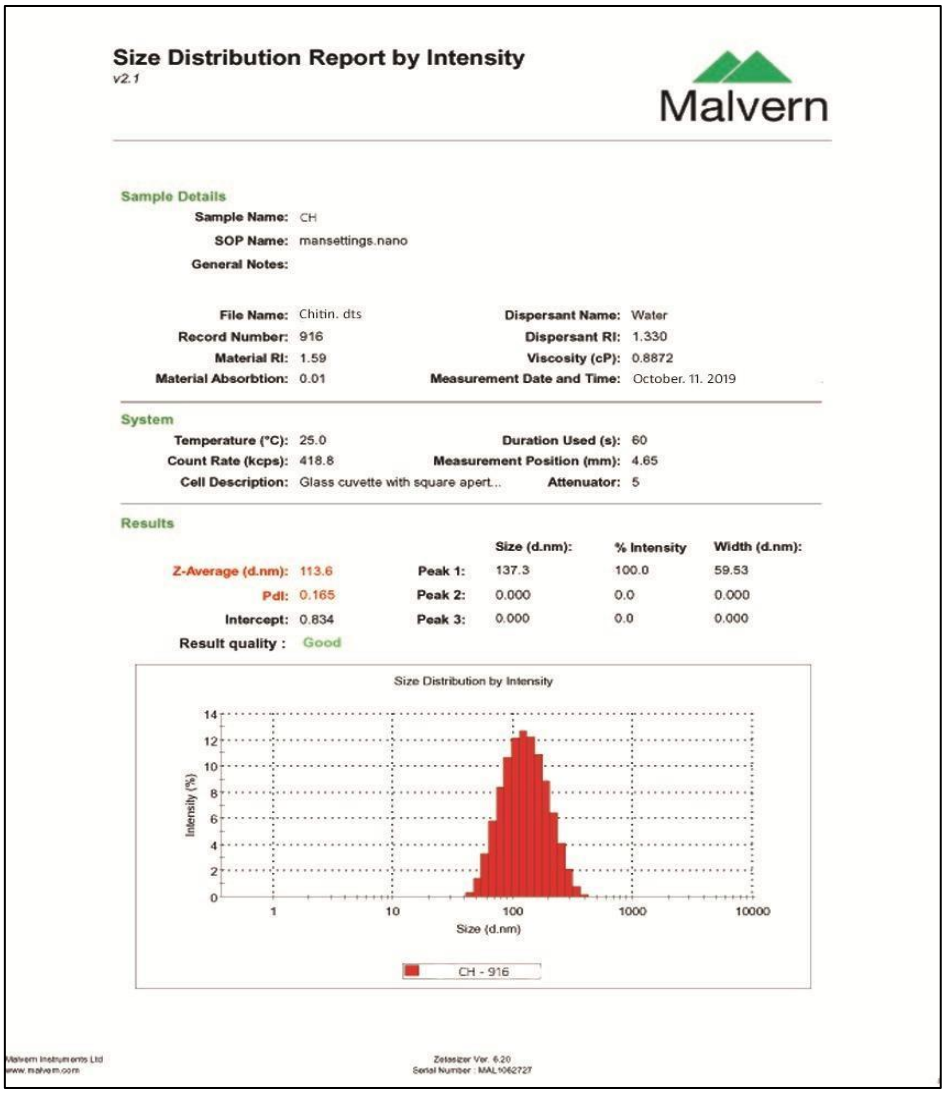


Fig. 15 (b) DLS analysis of AuNPs

The DLS analysis of the AuNPs showed a narrow, homogeneous size distribution with an average hydrodynamic diameter of 51.43 nm, indicating a monodisperse colloidal system. The hydrodynamic diameter determined by DLS includes the chitosan capping layer, which explains why it is larger than the core sizes observed by TEM and AFM (Geertsen *et al*., 2018). Polydispersity index values below 0.3 are considered indicative of good monodispersity in nanoparticle formulations, consistent with the distribution observed here (Mohan *et al*., 2019).

3.10 Antibacterial Activity

Using the disc diffusion technique, the antibacterial activity of the aqueous extract of chitosan and gold-synthesized nanoparticles (AuNPs) was assessed against the Gram-positive bacteria *E. faecalis* and S. aureus and the Gram-negative bacteria *E. coli*, *Enterobacter*, *P. aeruginosa*, and *K. pneumonia*e. Amikacin was used as a standard. Experimental results were

expressed as mean ± standard error and deviation. In the present study, the aqueous chitosan extract was found to be more effective against both Gram-negative and Gram-positive microorganisms. ATCC culture strains showed maximum zone of inhibition for *K. pneumonia* such as (18± 0.45mm) at 10 to 40µg/ ml followed by *P. aeruginosa* (16 ±0.58mm) and *E. faecalis* (16 ± 0.77mm), *S.aureus* (15 ±0.57mm), *E. coli* (12±0.66mm) and then *Enterobacter* (10 ±0.59mm) . The zone of inhibition formed was recorded on the plate. Similar results were observed for Gram-negative *P. aeruginosa* (16 ±0.58mm) and Gram-positive *E. faecalis* (16 ± 0.77mm) organisms. Table. 4 represents the results of AuNPs, which showed maximum zone of inhibition for *S.aureus* (22 ±0.77mm) at 40µg/ml and *P. aeruginosa* (22 ±1.47mm) and minimum zone for *Enterobacter* (12 ±0.69mm) were noticed. Zone of inhibition formed was given in the Plate.1. In general AuNPs was more effective against both the bacterial strains than the aqueous extract of chitosan. For clinical strains, the aqueous extract showed the largest zone of inhibition against *Enterobacter*iaceae, including *E. coli*. When compared against *E. coli* treated with AuNPs, *Enterobactor* showed a higher zone of inhibition (18 ±0.43mm), and *E. faecalis* and *P. aeruginosa* showed more or less similar zones of inhibition was found to be present i.e around (16 ± 1.76mm to 1.76 mm) . When the concentration increased, the zone of inhibition also increased. This study found that, for both ATCC and clinical strains, AuNPs were more effective than chitosan aqueous extracts.

3.10.1 Antibacterial activity of chitosan aqueous extract against various ATCC strains

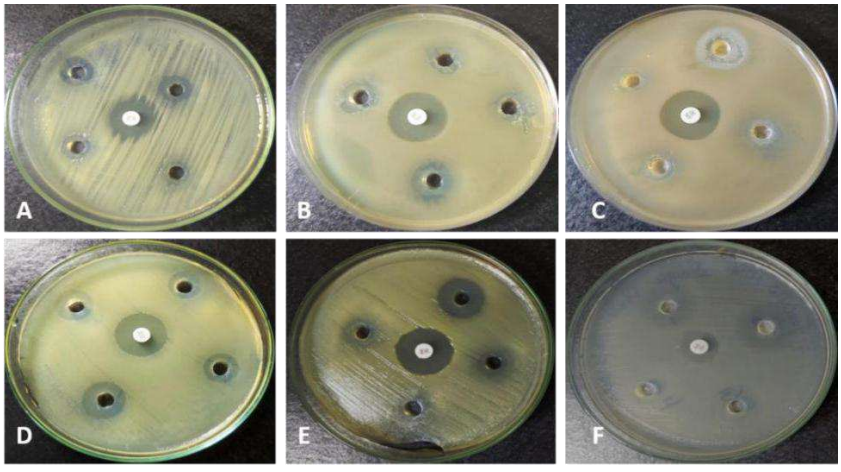


Plate -1: Photograph showing the discs of antibacterial activity of chitosan aqueous extract against various ATCC strains A) *E. coli*, B) *Enterobacter*, C) *P. aeruginosa*, D) *K. pneumonia*e E) S. aureus, F) *E. faecalis*

Table -1: Antibacterial activity of chitosan aqueous extract against various ATCC strains

(µg/ml)

	Zone of inhibition (mm)				
Test Organism	**Amikacin (Control)**	Concentration µg/ml			
		10 µg/ml	**20 µg/ml**	**30 µg/ml**	**40 µg/ml**
E. coli	14±0.83	**14±0.83**	**2±0.66**	**7±0.68**	**10±0.63**
Enterobacter	20±0.76	**20±0.76**	**6±0.59**	**8±0.85**	**9±0.57**
P. aeruginosa	22±0.88	**22±0.88**	**7±0.49**	**6±0.79**	**8±0.69**
K. pneumoniae	18±0.79	**18±0.79**	**8±0.78**	**12±0.75**	**15±0.53**
S. aureus	20±0.85	**20±0.85**	**6±0.85**	**8±0.76**	**13±0.45**
E.faecalis	14±0.65	**14±0.65**	**6±0.59**	**8±0.57**	**12±0.76**

Values are mean ± S.E. of six individual observations.

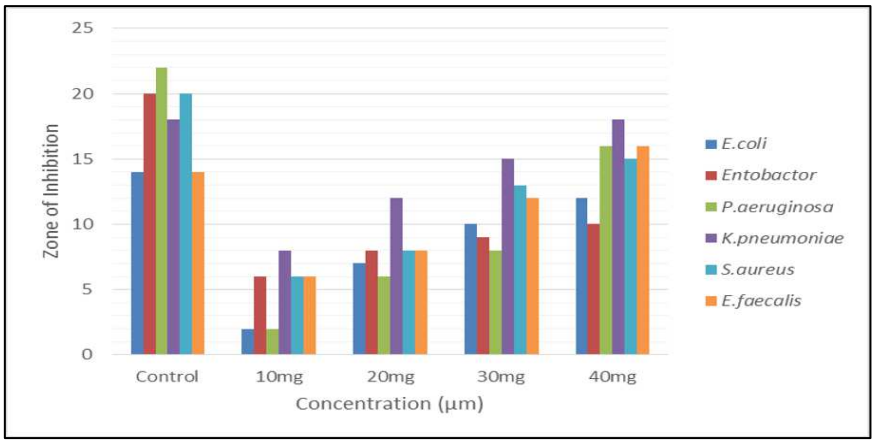


Fig. 16 Antibacterial activity of chitosan aqueous extract against various ATCC strains

Plate 1, Table 1, and Fig. 16 showcase an agar-well diffusion assay that produced clear zones of inhibition against all six ATCC strains, with activity increasing dose-dependently from 10 to 40 µg/mL; the greatest effect was recorded against *K. pneumonia*e (18 ± 0.45 mm). This method relies on diffusion of the test agent through the agar, and measurable inhibition zones confirm antibacterial efficacy, as demonstrated for various nanoparticle formulations in the literature (Shikha *et al*., 2020). The generally stronger effects against Gram-positive organisms reflect the known susceptibility of their single-layer cell wall to chitosan-mediated disruption (Shahzadi *et al*., 2018). *Enterobactor* showed remarkable activity when compared with the known standard, amikacin. A similar zone of inhibition was noticed in *Enterobactor* and the standard control, amikacin.

3.10.2 Antibacterial activity of Chitosan-mediated AuNPs against ATCC strains

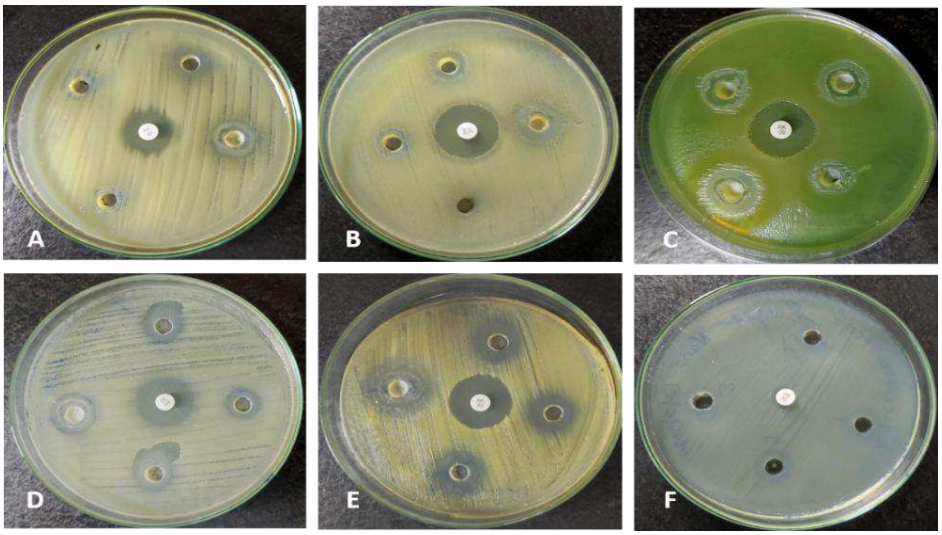


Plate -2: Photograph showing the discs of antibacterial activity of Chitosan-mediated AuNPs against ATCC strains A) E.coli, B) *Enterobacter*, C) *P. aeruginosa*, D) *K. pneumonia*e, E)*S.aureus*, F) E.faecalis

	Zone of inhibition (mm)				
Test Organisms	**Amikacin (Control)**	Concentration µg/ml			
		10 **µg/ml**	**20 µg/ml**	**30 µg/ml**	**40 µg/ml**
E. coli	20±0.45	2±0.55	8±0.45	12±0.54	16±1.62
Enterobacter	13±0.12	5±0.75	8±1.03	10±0.30	12±0.69
P. aeruginosa	22±0.47	8±0.92	12±0.12	16±0.12	22±1.47
K. pneumoniae	18±0.67	8±1.12	12±0.54	14±0.45	15±0.61
S. aureus	23±0.78	10±0.74	12±0.23	18±0.53	22±0.77
E.faecalis	12±0.93	4±0.54	16±0.45	12±0.32	16±0.12

Table -2: Antibacterial activity of Chitosan-mediated AuNPs against various ATCC strains (µg/ml)

Values are mean ± S.E. of six individual observations.

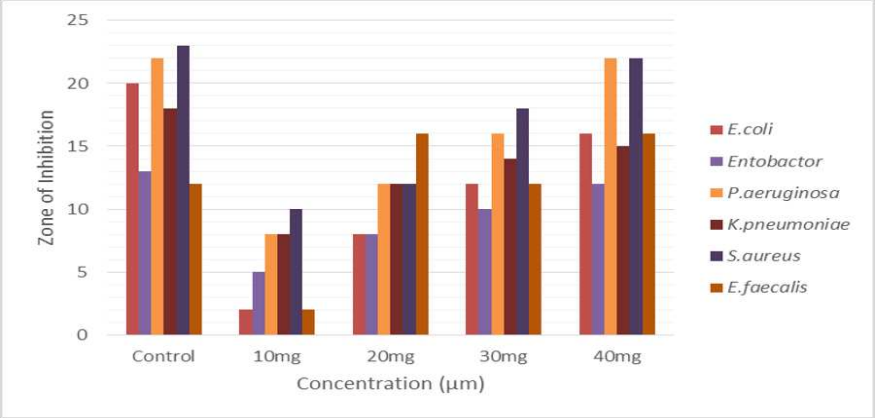


Fig. 17 Antibacterial activity of Chitosan-mediated AuNPs against various ATCC strains

The AuNPs produced larger zones of inhibition than the chitosan extract, with maximum activity against S. aureus (22 ± 0.77 mm) and *P. aeruginosa* (22 ± 1.47 mm) at 40 µg/mL. Chitosan-capped AuNPs have been reported to inhibit both *P. aeruginosa* and S. aureus in agar-well assays, and the enhancement in activity over the free polymer confirms that the AuNP–chitosan complex is responsible for the effect (Fathil *et al*., 2022). Comparable zone diameters (e.g., ~22 mm against S. aureus) have been documented for green-Chitosan-mediated AuNPs against Gram-positive and Gram-negative pathogens (Shafiq *et al*., 2021). Plate 2, Table 2, and Fig. 17 showcase the antibacterial activity of Chitosan-mediated AuNPs against various ATCC strains.

3.10.3 Antibacterial activity of aqueous chitosan extract against various clinical strains

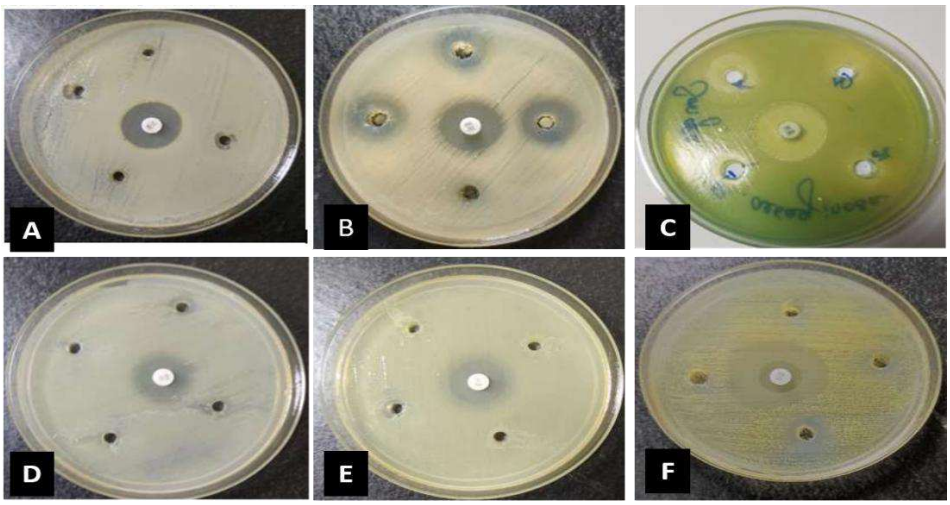


Plate -3: Photograph showing the discs of antibacterial activity of aqueous chitosan extract against various clinical strains A) E.coli, B) *Enterobacter*, C) *P. aeruginosa*, D) *K. pneumonia*e, E) *S.aureus*, F) E.faecalis

	Zone of inhibition (mm)				
Test Organisms	**Amikacin (Control)**	Concentration µg/ml			
		10 **µg/ml**	20 **µg/ml**	30 **µg/ml**	40 **µg/ml**
E. coli	12±0.43	2±0.39	2±0.45	8±0.68	6±0.54
Enterobacter	18±0.55	3±0.47	10±0.43	14±0.47	17±0.58
P. aeruginosa	20±0.34	5±0.54	6±0.10	8±0.57	15±0.76
K. pneumoniae	14±0.63	4±0.65	2±0.76	7±0.67	2±0.34
S. aureus	17±0.56	8±0.45	9±0.52	6±0.93	2±0.46
E.faecalis	15±0.46	9±0.56	8±0.45	9±0.48	14±0.54

Table -3: Antibacterial activity of chitosan aqueous extract against various clinical strains (µg/ml)

Values are mean ± S.E. of six individual observations.

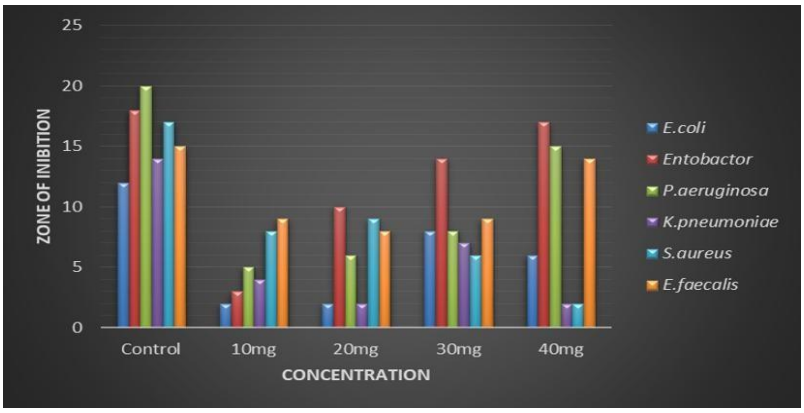


Fig. 18 Antibacterial activity of chitosan aqueous extract against various clinical strains

Against clinical isolates, the extract showed the strongest inhibition of *Enterobacter* (17 ± 0.58 mm), followed by *P. aeruginosa* and *E. faecalis*, with the zone size increasing with concentration. These results demonstrate the potential of chitosan against clinically relevant, possibly multidrug-resistant strains, an area of growing interest given the limited efficacy of conventional antibiotics against resilient pathogens (Azzam *et al*., 2024). Plate 3, Table 3 and Fig 18 showcase the antibacterial activity of chitosan aqueous extract against various clinical strains.

3.10.4 Antibacterial activity of Chitosan-mediated AuNPs against clinical strains

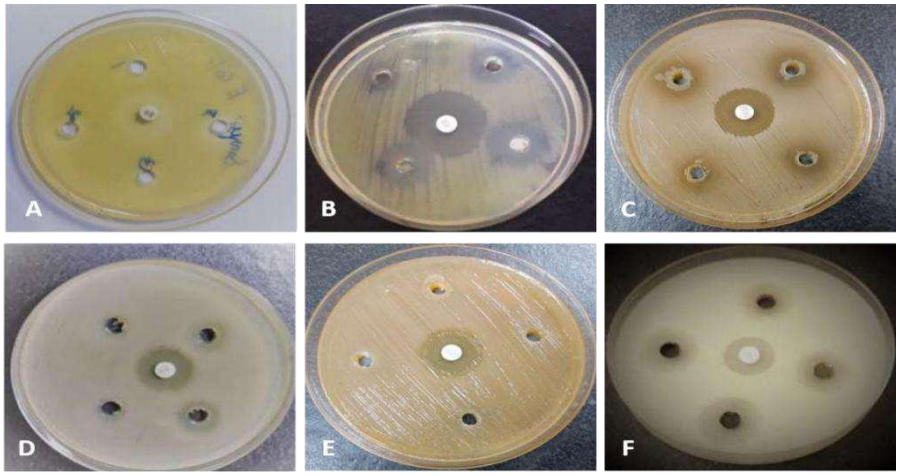


Plate -4: Photograph showing the discs of antibacterial activity of Chitosan-mediated AuNPs against clinical strains. A) *E. coli*, B) *Enterobacter*, C) *P. aeruginosa*, D) *K. pneumonia*e E) *S.aureus*, F) E.faecalis

	Zone of inhibition (mm)				
Test Organisms	**Amikacin (Control)**	Concentration µg/ml			
		10 **µg/ml**	20 **µg/ml**	30 **µg/ml**	40 **µg/ml**
E. coli	12±0.33	2±0.42	2±0.47	2±0.36	6±0.56
Enterobacter	18±0.22	5±0.28	10±0.40	14±0.74	18±0.43
P. aeruginosa	20±0.12	2±0.83	06±1.32	8±0.65	16±1.76
K. pneumoniae	14±0.88	8±0.49	02±0.86	10±0.54	2±0.37
S. aureus	17±0.43	4±0.78	03±0.49	8±0.59	3±0.58
E.faecalis	15±0.34	6±0.68	08±1.08	10±0.68	16±0.79

Table -4: Antibacterial activity of Chitosan-mediated AuNPs against various Clinical strains (µg/ml)

Values are mean ± S.E. of six individual observations.

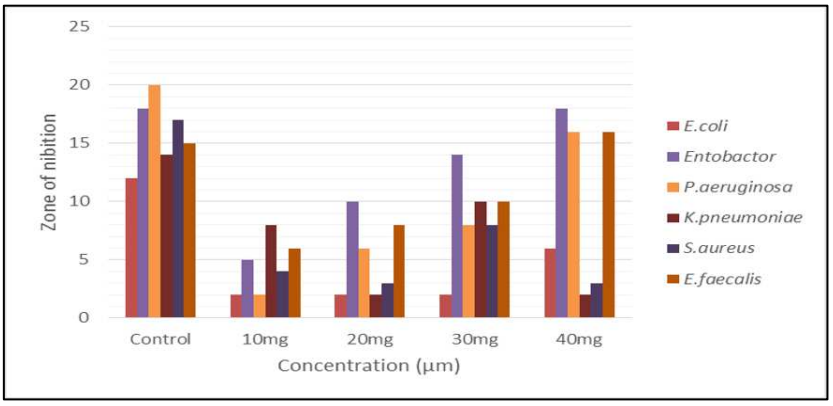


Fig. 19 Antibacterial activity of Chitosan-mediated AuNPs against various Clinical strains

The AuNPs exhibited higher zones of inhibition against clinical strains, with *Enterobacter* reaching 18 ± 0.43 mm at 40 µg/mL. Biosynthesized gold nanoparticles exhibit pronounced activity against clinical and hospital-acquired bacterial isolates, including multidrug-resistant strains, and their mechanism of action — unlike that of antibiotics — targets multiple cellular targets, reducing the likelihood of resistance development (Azzam *et al*., 2024; Shikha *et al*., 2020) Plate 4, Table 4 and Fig 19 showcase the antibacterial activity of Chitosan-mediated AuNPs against various Clinical strains

3.11 Antifungal activity by the agar well diffusion method.

Antifungal activity by the agar well diffusion method. Sabouraud's dextrose agar was prepared and sterilized at 121˚C. The medium was poured on sterile Petri plates and allowed to solidify. The inoculum was prepared and adjusted to the McFarland 0.5 standard. Lawn culture was made on Potato Dextrose Agar plates and allowed to dry for 10 minutes. Prepared AgNPs and crude extracts (2.0 mg/mL) were loaded into the respective wells in agar plates. The plates were incubated at room temperature for 48-72 hours. After the incubation, the zone of inhibition was measured in mm.

3.11.1 Anti-fungal activity

Using the agar well diffusion technique, the antifungal activity of the aqueous extract and synthesized chitosan AuNPs was investigated against the fungal strains *A. niger*, *Penicillium*, *Rhizopus*, and *A. flavus*. Fluconazole was used as a control. The aqueous chitosan extract showed

no significant differences in antifungal activity against *A.flavus* (14±0.43 mm) at 40 µg /ml, followed by *Penicillium* (12±0.22 mm), *Rhizopus* (11±0.33 mm), and *A.niger* (04±0.13mm). The zone of inhibition formed was measured in mm and increased in a dose-dependent manner . The results of the study indicated that various concentrations of AuNPs inhibited fungal growth of strains,nd the inhibition increased with increasing concentration of NPs. AuNPs revealed higher antifungal activity for *Penicillium*, with a zone of inhibition (15±0.57 mm) at 40 µg /ml, followed by *A.niger* (14±0.65 mm), *A.flavus* (14mm±0.36mm), and *Rhizopus* (13mm±0.72mm). Thus, antifungal activity was observed in AuNPs compared with the chitosan aqueous extract.

3.11.1. 1 Antifungal activity of chitosan aqueous extract

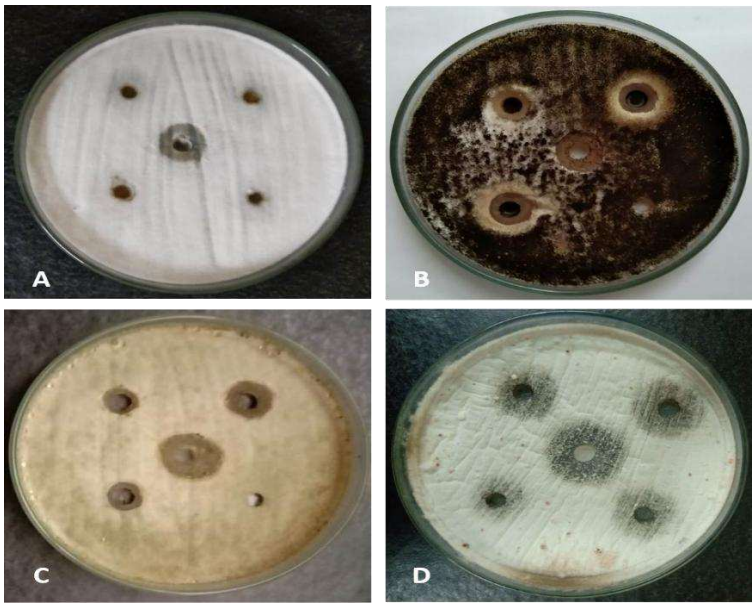


Plate -5: Photograph showing the discs of antifungal activity of chitosan aqueous extract A) *A. niger*, B) *Penicillium*, C) *Rhizopus*, D) *A.flavus*

The aqueous extract inhibited the four test fungi in a dose-dependent manner, with the largest zone against *A. flavus* (14 ± 0.43 mm) at 40 µg/mL, followed by *Penicillium*, *Rhizopus*, and *A. niger*. Antifungal activity measured as zones of inhibition around wells is the standard metric in such assays, and metallic nanoparticle–polymer systems have repeatedly shown activity

	Zone of inhibition (mm)				
Test Organisms	**Fluconazole (Control)**	**Concentration µg/ml**			
		10 µg/ml	**20 µg/ml**	**30 µg/ml**	**40 µg/ml**
A.niger	**13±15**	**02±0.5**	**03±0.5**	**05±0.12**	**04±0.13**
Penicillium	**12±15**	**07±0.22**	**09±0.25**	**10±0.12**	**12±0.22**
Rhizopus	**14±20**	**05±0.21**	**07±0.32**	**10±0.23**	**11±0.33**
A. flavus	**16±20**	**11±0.33**	**12±0.22**	**14±0.34**	**14±0.43**

Table -5: Antifungal activity of chitosan aqueous extract against various fungal strains (µg/ml)

Values are mean ± S.E. of six individual observations.

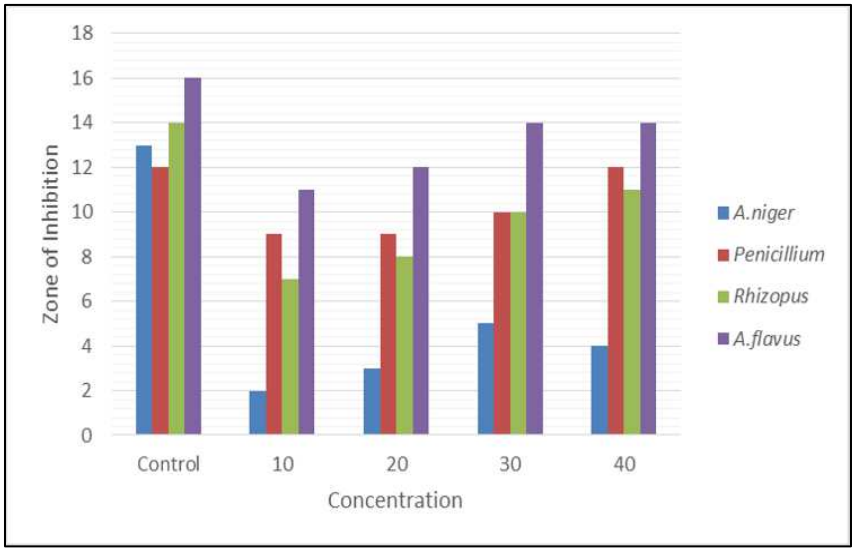


Fig. 20 Antifungal activity of chitosan aqueous extract against various fungal strains

The AuNPs showed superior antifungal activity compared with the extract, with the largest zone against *Penicillium* (20 ± 0.57 mm), followed by *A. niger* (15 ± 0.65 mm), *A. flavus* (15 ± 0.36 mm) and *Rhizopus* (13 ± 0.72 mm) at 40 µg/mL. Greater zones of inhibition at higher

nanoparticle concentrations — as observed here — are consistent with reports that increasing nanoparticle dose enhances antifungal efficacy against *Penicillium*, *Rhizopus*, and Aspergillus (Ahmad *et al*., 2024). The smaller zones obtained with larger particles (≈50 nm here) also align with the size-dependence of antifungal action (Nguyen *et al*., 2022). Plate 5, Table 5 and Fig. 20 antifungal activity of chitosan aqueous extract against various fungal strains.

3.11.1.2 Antifungal activity of AuNPs

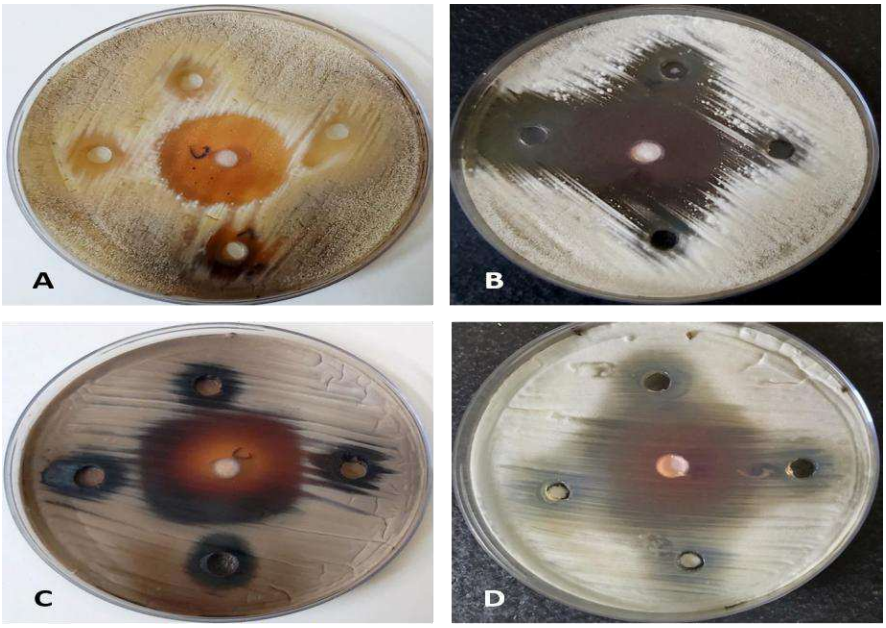


Plate -6: Photograph showing the discs of antifungal activity of AuNPs niger, B) *Penicillium*, C) *Rhizopus* D) *A.flavus*

The agar-well diffusion assay produced clear, concentration-dependent zones of inhibition by the Chitosan-mediated AuNPs against all four test fungi, with activity increasing progressively from 10 to 40 µg/mL across all strains. The highest zone was recorded against *Penicillium* (20 ± 0.57 mm at 40 µg/mL), followed by *A. niger* (15 ± 0.65 mm), *A. flavus* (15 ± 0.36 mm), and *Rhizopus* (13 ± 0.72 mm) (Ahmad *et al*., 2024). This dose-dependent response mirrors reports for other biogenic gold nanoparticles, where zone diameters against *A. flavus* and *A. niger* increased steadily with nanoparticle concentration (e.g., 5→9 mm for *A. flavus* and 5→9 mm for *A. niger* as the dose rose from 10 to 50 µg/mL) (Piruthiviraj *et al*., 2015). The zone sizes obtained here are also comparable to those documented for gold nanoparticles against the same species — AuNPs produced zones of 14 mm against *A. flavus* and 12 mm against *A. niger* in a study on onychomycosis isolates (Sami, 2019). Notably, *Penicillium* proved the most susceptible of the four genera, in agreement with findings that gold-containing nanoparticles tested simultaneously against *A. niger*, *A. flavus*, *Rhizopus*, and *Penicillium* showed the largest zone against *Penicillium*

(25 mm at 40 µL) (Fathima *et al*., 2021). Overall, the AuNPs outperformed the chitosan aqueous extract, confirming that the AuNP-capped chitosan complex, rather than the polymer alone, is responsible for the enhanced antifungal efficacy. The moderate zone diameters observed here are consistent with the manuscript's own observation that the ~50 nm particle size limits antifungal potency, since smaller particles (<100 nm) have been reported to be more effective antifungal agents. Plate 6, Table 6 and Fig. 21 showcases the antifungal activity of AuNPs against various fungal strains (µg/ml).

	Zone of inhibition (mm)				
Test Organisms	**Fluconazole (Control)**	**Concentration**			
		10 µg/ml	**20 µg/ml**	**30 µg/ml**	**40 µg/ml**
A.niger	**19±0.22**	**09±0.08**	**10±1.65**	**11±0.63**	**14±0.65**
Penicillium	**22±0.66**	**09±0.66**	**09±0.77**	**10±0.65**	**15±0.57**
Rhizopus	**29±0.72**	**09±1.03**	**10±0.74**	**10±0.69**	**13±0.72**
A.flavus	**24±0.83**	**11±0.66**	**12±0.91**	**12±0.48**	**14±0.36**

Table- 6: Antifungal activity of AuNPs against various fungal strains (µg/ml)

Values are mean ± S.E. of six individual observations.

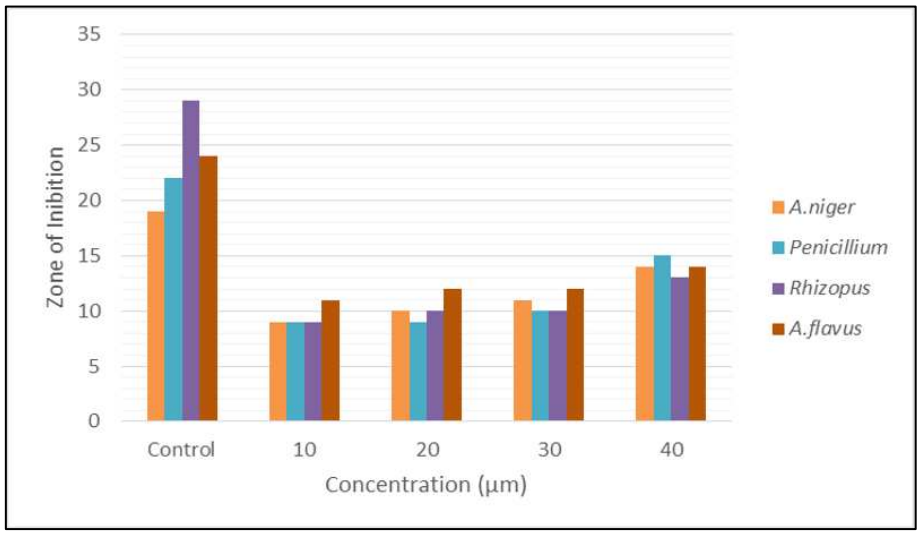


Fig. 21 Antifungal activity of AuNPs against various fungal strains Caption: Bar chart showing the zone of inhibition (mm) of Chitosan-mediated AuNPs against A) *A. niger*, B) *Penicillium*, C) *Rhizopus* and D) *A. flavus* at 10–40 µg/mL by the agar well diffusion method.

The bar chart illustrates the dose-dependent antifungal activity of the synthesized chitosan-based AuNPs against four fungal strains (*A. niger*, *Penicillium*, *Rhizopus* and *A. flavus*) at concentrations of 10, 20, 30 and 40 µg/mL, measured as the zone of inhibition in millimeters (mean ± S.E. of six observations, Table 6) . The inhibition zones increased progressively with rising nanoparticle concentration for all four strains: *A. niger* from 09 ± 0.08 mm to 14 ± 0.65 mm, *Penicillium* from 09 ± 0.66 mm to 15 ± 0.57 mm, *Rhizopus* from 09 ± 1.03 mm to 13 ± 0.72 mm, and *A. flavus* from 11 ± 0.66 mm to 14 ± 0.36 mm. The greatest activity at 40 µg/mL was recorded against *Penicillium* (15 ± 0.57 mm), followed by *A. niger* (14 ± 0.65 mm), *A. flavus* (14 ± 0.36 mm), and *Rhizopus* (13 ± 0.72 mm) (Plate 6 and Table 6). This concentration-dependent enhancement matches findings for other green-synthesized gold nanoparticles, whose zones against *A. flavus* and *A. niger* increased steadily with dose — e.g., 5 → 9 mm and 5 → 9 mm as the concentration rose from 10 to 50 µg/mL (Piruthiviraj *et al*., 2015). It is also consistent with a study on Annona muricata-derived AuNPs, in which the highest antifungal activity was observed against *Penicillium* (66% inhibition), and (Fig. 21) efficacy increased with increasing nanoparticle concentration (Folorunso *et al*., 2019). Gold-containing nanoparticles tested against these same genera have likewise produced clear zones of inhibition against *A. niger*, *A. flavus*, *Rhizopus*, and *Penicillium* (Fathima *et al*., 2021). The proposed mechanism underlying such activity involves interaction of the nanoparticles with the fungal membrane, causing pore formation that leads to cell death (Fathima *et al*., 2021). As discussed in the present manuscript, the moderate zone diameters can be attributed to the relatively large (~50 nm) particle size, since smaller particles (below 100 nm) are reported to be more effective antifungal agents — which also explains why the AuNPs showed only marginal improvement over the chitosan extract against some strains.

4. FUNDING DECLARATION

The authors declare that no funds or grants were received during the research work and preparation of this manuscript.

5. CONCLUSION

This study successfully demonstrates the eco-friendly biosynthesis of chitosan-gold nanoparticles (CHS-AuNPs) using chitosan extracted from crab shell waste of *Portunus sanguinolentus*. The comprehensive characterization through UV-Vis spectroscopy, FT-IR, XRD, SEM-EDX, HR-TEM with SAED, DLS, and AFM confirmed the successful formation of crystalline, spherical nanoparticles with average sizes ranging from 8–51 nm. The CHS-AuNPs exhibited significant dose-dependent antimicrobial activity against both Gram-positive and Gram-

negative bacterial strains, as well as antifungal activity against common fungal pathogens. The enhanced antimicrobial efficacy of CHS-AuNPs compared to chitosan alone highlights their potential as promising therapeutic agents. The use of marine crustacean waste for nanoparticle synthesis offers a sustainable, cost-effective approach that addresses both environmental pollution and biomedical needs. These findings suggest that CHS-AuNPs could serve as novel therapeutic agents in biomedical applications, particularly in drug delivery systems and infection control, warranting further investigation for clinical applications.

6. REFERENCES

1. Dhillon, G. S., Kaur, S., Brar, S. K., & Verma, M. (2013) . Green synthesis approach: extraction of chitosan from fungus mycelia. Critical reviews in biotechnology, 33(4), 379-403.
2. Manivasagan, P., & Oh, J. (2016) . Marine polysaccharide-based nanomaterials as a novel source of nanobiotechnological applications. International journal of biological macromolecules, 82, 315-327.
3. Murugan, K., Anitha, J., Suresh, U., Rajaganesh, R., Panneerselvam, C., Aziz, A. T., ... & Hwang, J. S. (2017) . Chitosan-fabricated Ag nanoparticles and larvivorous fishes: a novel route to control the coastal malaria vector Anopheles sundaicus?. Hydrobiologia, 797(1), 335-350.
4. Affes, S., Maalej, H., Aranaz, I., Kchaou, H., Acosta, N., Heras, Á., & Nasri, M. (2020) . Controlled size green synthesis of bioactive silver nanoparticles assisted by chitosan and its derivatives and their application in biofilm preparation. Carbohydrate polymers, 236, 116063.
5. Chen, X., Zhao, X., & Wang, G. (2020) . Review on marine carbohydrate-based gold nanoparticles represented by alginate and chitosan for biomedical application. Carbohydrate Polymers, 244, 116311.
6. Kalaivani, R., Maruthupandy, M., Mun eeswaran, T., Singh, M., Sureshkumar, S., Anand, M., ... & Kumaraguru, A. K. (2020) . Chitosan mediated gold nanoparticles against pathogenic bacteria, fungal strains and MCF-7 cancer cells. International journal of biological macromolecules, 146, 560-568.
7. Begum, S., Yuhana, N. Y., Saleh, N. M., Kamarudin, N. N., & Sulong, A. B. (2021) . Review of chitosan composite as a heavy metal adsorbent: Material preparation and properties. Carbohydrate Polymers, 117613.

8. Emam, H. E., Ahmed, H. B., & Abdelhameed, R. M. (2021) . Melt intercalation technique for synthesis of hetero-metallic@ chitin bio-composite as recyclable catalyst for prothiofos hydrolysis. Carbohydrate Polymers, 266, 118163.

9. Hajji, S., Kchaou, H., Bkhairia, I., Salem, R. B. S. B., Boufi, S., Debeaufort, F., & Nasri, M. (2021) . Conception of active food packaging films based on crab chitosan and gelatin enriched with crustacean protein hydrolysates with improved functional and biological properties. Food Hydrocolloids, 116, 106639.

10. Novais, G. B., Santana, R. J. R., Carvalhal, K. S., da Silva Júnior, E. F., Melo, C. M., Severino, P., & Cardoso, J. C. (2021) . Novel processes combining natural products and synthetic materials for developing nanolarvicides. In Applications of Nanobiotechnology for Neglected Tropical Diseases (pp. 477-492) . Academic Press.

11. Salomatina, E. V., Fukina, D. G., Koryagin, A. V., Titaev, D. N., Suleimanov, E. V., & Smirnova, L. A. (2021) . Preparation and photocatalytic properties of titanium dioxide modified with gold or silver nanoparticles. Journal of Environmental Chemical Engineering, 9(5), 106078.

12. Fathi, M., M. K. Ahmed, M. Afifi, A. A. Menazea, and Vuk Uskoković. ACS Biomater. Sci. Eng. 2021, 7, 1, 360–372 Publication Date:December 18, 2020 https://doi.org/10.1021/acsbiomaterials.0c01105

13. Tommalieh, M.J., Ismail, A.M., Awwad, N.S. *et al.* Investigation of Electrical Conductivity of Gold Nanoparticles Scattered in Polyvinylidene Fluoride/Polyvinyl Chloride via Laser Ablation for Electrical Applications. *J. Electron. Mater.* 49, 7603–7608 (2020) . https://doi.org/10.1007/s11664-020-08459-2

14. Menazea, A.A., Mohamed H. El-Newehy, Badr M. Thamer, Mehrez E. El-Naggar, Preparation of antibacterial film-based biopolymer embedded with vanadium oxide nanoparticles using one-pot laser ablation, Journal of Molecular Structure, 1225, 2021, 129163, https://doi.org/10.1016/j.molstruc.2020.129163.

15. Abd El-Kader, M.F.H., M.K. Ahmed, M.T. Elabbasy, M. Afifi, A.A. Menazea, Morphological, ultrasonic mechanical and biological properties of hydroxyapatite layers deposited by pulsed laser deposition on alumina substrates, Surface and Coatings Technology, 409, 2021, 126861, https://doi.org/10.1016/j.surfcoat.2021.126861.

16. Elabbasy, M.T., M.F.H. Abd El-Kader, A.M. Ismail, A.A. Menazea, Regulating the function of bismuth (III) oxide nanoparticles scattered in Chitosan/Poly (Vinyl Pyrrolidone) by laser ablation on electrical conductivity characterization and antimicrobial activity, Journal of Materials Research and Technology, 10, 2021, 1348-1354, https://doi.org/10.1016/j.jmrt.2020.12.109.

17. Al Mogbel, M. S., Elabbasy, M. T., Mohamed, R. S., Ghoniem, A. E., El-Kader, M. F. H. A., & Menazea, A. A. (2021) . Improvement in antibacterial activity of Poly Vinyl Pyrrolidone/Chitosan incorporated by graphene oxide NPs via laser ablation. Journal of Polymer Research, 28(12), Article 474. https://doi.org/10.1007/s10965-021-02838-x.

18. Alzahrani, E., Shaltout, A.A., Moustapha, M.E. *et al.* Optical, structural, and electrical conductivity of PEO/chitosan incorporated by Se NPs produced by one-potential laser ablation. *J Mater Sci: Mater Electron* 33, 12351–12358 (2022) .

19. Kyzas, G. Z., & Bikiaris, D. N. (2015) . Recent modifications of chitosan for adsorption applications: A critical and systematic review. *Marine Drugs, 13*(1), 312–337. https://doi.org/10.3390/md13010312

20. Younes, I., & Rinaudo, M. (2015) . Chitin and chitosan preparation from marine sources: Structure, properties and applications. Marine Drugs, 13(3), 1133–1174. https://doi.org/10.3390/md13031133

21. Zargar, V., Asghari, M., & Dashti, A. (2015) . A review on chitin and chitosan polymers: Structure, chemistry, solubility, derivatives, and applications. ChemBioEng Reviews, 2(3), 204–226. https://doi.org/10.1002/cben.201400025

22. Santos, V. P., Marques, N. S. S., Maia, P. C. S. V., Lima, M. A. B. de, Franco, L. de O., & Campos-Takaki, G. M. de. (2020) . Seafood waste as attractive source of chitin and chitosan production and their applications. International Journal of Molecular Sciences, 21(12), 4290. https://doi.org/10.3390/ijms21124290

23. Sivanesan, I., Gopal, J., Muthu, M., Shin, J., Mari, S., & Oh, J. (2021) . Green Synthesized Chitosan/Chitosan Nanoforms/Nanocomposites for Drug Delivery Applications. Polymers, 13(14), 2256.

24. Sun, X., Wu, Q., Picha, D. H., Ferguson, M. H., Ndukwe, I. E., & Azadi, P. (2021) . Comparative performance of bio-based coatings formulated with cellulose, chitin, and chitosan

nanomaterials suitable for fruit preservation. Carbohydrate Polymers, 259, 117764.

25. Lv, S., Zhou, H., Bai, L., Rojas, O. J., & McClements, D. J. (2021) . Development of food-grade Pickering emulsions stabilized by a mixture of cellulose nanofibrils and nanochitin. Food Hydrocolloids, 113, 106451.

26. Pradhan, J., Baisakhi, B., Das, B. K., Jena, K., Ananta, S., & Mohanty, D. (2024) . Chitosan extracted from *Portunus sanguinolentus* (three-spot swimming crab) shells: Its physico-chemical and biological potentials. *Journal of Environmental Biology, 45*(1), 62–71. https://doi.org/10.22438/jeb/45/1/MRN-S186

27. Amoo, K. O., Olafadehan, O. A., & Ajayi, T. O. (2019) . Optimization studies of chitin and chitosan production from *Penaeus notialis* shell waste. *African Journal of Biotechnology, 18*(27), 670–688. https://doi.org/10.5897/AJB2019.16861

28. Mohan, C. O., Gunasekaran, S., & Ravishankar, C. N. (2019) . Chitosan-capped gold nanoparticles for indicating temperature abuse in frozen stored products. *npj Science of Food, 3*(1), 2. https://doi.org/10.1038/s41538-019-0034-z

29. Cazacu, A., Dobromir, M., Chiruță, C., & Ursu, E.-L. (2022) . Chitosan-mediated environment-friendly synthesis of gold nanoparticles with enhanced photonic reactivity. *Nanomaterials, 12*(23), 4186. https://doi.org/10.3390/nano12234186

30. Fathil, M. A. M., Taufeq, F. Y. F., Abdalla, S. S. I., & Katas, H. (2022) . Roles of chitosan in synthesis, antibacterial and anti-biofilm properties of bionano silver and gold. *RSC Advances, 12*(30), 19297–19312. https://doi.org/10.1039/d2ra01734b

31. Hao, G., Hu, Y., Shi, L., Chen, J., Cui, A., Weng, W., & Osako, K. (2021) . Physicochemical characteristics of chitosan from swimming crab (*Portunus trituberculatus*) shells prepared by subcritical water pretreatment. *Scientific Reports, 11*(1), 1646. https://doi.org/10.1038/s41598-021-81318-0

32. Katas, H., Lim, C. S., Nor Azlan, A. Y. H., Buang, F., & Mh Busra, M. F. (2019) . Antibacterial activity of biosynthesized gold nanoparticles using biomolecules from *Lignosus rhinocerotis* and chitosan. *Saudi Pharmaceutical Journal, 27*(2), 283–292. https://doi.org/10.1016/j.jsps.2018.11.010

33. Corazzari, I., Nisticò, R., Turci, F., Faga, M. G., Franzoso, F., Tabasso, S., & Magnacca, G. (2015) . Advanced physico-chemical characterization of chitosan by means of TGA coupled on-line with FTIR and GCMS: Thermal degradation and water adsorption capacity. *Polymer Degradation and Stability, 112*, 1–9. https://doi.org/10.1016/j.polymdegradstab.2014.12.006

34. Takara, E. A., Marchese, J., & Ochoa, N. A. (2015) . NaOH treatment of chitosan films: Impact on macromolecular structure and film properties. *Carbohydrate Polymers, 132*, 25–30. https://doi.org/10.1016/j.carbpol.2015.05.077

35. Boruah, J. S., Devi, C., Hazarika, U., Reddy, P. V. B., Chowdhury, D., Barthakur, M., & Kalita, P. (2021) . Green synthesis of gold nanoparticles using an antiepileptic plant extract: *In vitro* biological and photo-catalytic activities. *RSC Advances, 11*(45), 28029–28041. https://doi.org/10.1039/d1ra02669k

36. Wu, C.-C., & Chen, D.-H. (2010) . Facile green synthesis of gold nanoparticles with gum arabic as a stabilizing agent and reducing agent. *Gold Bulletin, 43*(4), 234–240. https://doi.org/10.1007/BF03214993

37. Choudhary, R. C., Kumaraswamy, R. V., Kumari, S., Sharma, S. S., Pal, A., Raliya, R., Biswas, P., & Saharan, V. (2017) . Cu-chitosan nanoparticle boost defense responses and plant growth in maize (*Zea mays* L.) . *Scientific Reports, 7*(1), 9754. https://doi.org/10.1038/s41598-017-08571-0

38. Joudeh, N., & Linke, D. (2022) . Nanoparticle classification, physicochemical properties, characterization, and applications: A comprehensive review for biologists. *Journal of Nanobiotechnology, 20*(1), 262. https://doi.org/10.1186/s12951-022-01477-8

39. Koliyote, S., & Shaji, J. (2023) . A recent review on synthesis, characterization and activities of gold nanoparticles using plant extracts. *Indian Journal of Pharmaceutical Education and Research, 57*(2s), s198–s212. https://doi.org/10.5530/ijper.57.2s.24

40. Nguyen, T. H. A., Nguyen, V.-C., Phan, T. N. H., Le, V. T., Vasseghian, Y., Trubitsyn, M. A., Nguyen, A.-T., Chau, T. P., & Doan, V.-D. (2022) . Novel biogenic silver and gold nanoparticles for multifunctional applications: Green synthesis, catalytic and antibacterial

activity, and colorimetric detection of Fe (III) ions. *Chemosphere, 287*(Part 3), 132271. https://doi.org/10.1016/j.chemosphere.2021.132271

41. Alhumaydhi, F. A., Khan, I., Rauf, A., Qureshi, M. N., Aljohani, A. S. M., Khan, S. A., Khalil, A. A., El-Esawi, M. A., & Muhammad, N. (2021) . Synthesis, characterization, biological activities, and catalytic applications of alcoholic extract of saffron (*Crocus sativus*) flower stigma-based gold nanoparticles. *Green Processing and Synthesis, 10*(1), 711–723. https://doi.org/10.1515/gps-2021-0066

42. Ghafoor, D. A., Yas, R. M., & Saeed, M. A. (2019) . The properties of nano-gold particles synthesized by ascorbic acid with acacia gum and sodium hydroxide as stabilizers. *Iraqi Journal of Science, 60*(10), 2149–2155. https://doi.org/10.24996/ijs.2019.60.10.7

43. Mytlak, F. A.-H. (2018) . Synthesis and characterization of Au nanoparticles for nanomedicine application. *Iraqi Journal of Physics, 15*(35), 109–116. https://doi.org/10.30723/ijp.v15i35.59

44. Zhou, C., Yu, J., Qin, Y., & Zheng, J. (2012) . Grain size effects in polycrystalline gold nanoparticles. *Nanoscale, 4*(14), 4228–4233. https://doi.org/10.1039/c2nr30212h

45. Mourdikoudis, S., Pallares, R. M., & Thanh, N. T. K. (2018) . Characterization techniques for nanoparticles: Comparison and complementarity upon studying nanoparticle properties. *Nanoscale, 10*(27), 12871–12934. https://doi.org/10.1039/c8nr02278j

46. Hans, R., Yadav, P. K., Zaman, M. B., Poolla, R., & Thavaselvam, D. (2023) . A rapid direct-differential agglutination assay for *Brucella* detection using antibodies conjugated with functionalized gold nanoparticles. *Frontiers in Nanotechnology, 5*, 1132783. https://doi.org/10.3389/fnano.2023.1132783

47. Geertsen, V., Barruet, E., Gobeaux, F., Lacour, J.-L., & Taché, O. (2018) . Contribution to accurate spherical gold nanoparticle size determination by single-particle inductively coupled mass spectrometry: A comparison with small-angle X-ray scattering. *Analytical Chemistry, 90*(16), 9742–9750. https://doi.org/10.1021/acs.analchem.8b00894

48. Zheng, T., Bott, S., & Huo, Q. (2016) . Techniques for accurate sizing of gold nanoparticles using dynamic light scattering with particular application to chemical and biological sensing

based on aggregate formation. *ACS Applied Materials & Interfaces, 8*(33), 21585–21594. https://doi.org/10.1021/acsami.6b06903

49. Shikha, S., Chaudhuri, S. R., & Bhattacharyya, M. S. (2020) . Facile one pot greener synthesis of sophorolipid capped gold nanoparticles and its antimicrobial activity having special efficacy against Gram negative *Vibrio cholerae*. *Scientific Reports, 10*(1), 1463. https://doi.org/10.1038/s41598-019-57399-3

50. Shahzadi, S., Zafar, N., & Sharif, R. (2018) . Antibacterial activity of metallic nanoparticles. In *Bacterial Pathogenesis and Antibacterial Control*. IntechOpen. https://doi.org/10.5772/intechopen.72526

51. Shafiq, T., Uzair, M., Iqbal, M. J., Zafar, M., Hussain, S. J., & Shah, S. A. A. (2021) . Green synthesis of metallic nano-particles and their potential in bio-medical applications. *Nano Biomedicine and Engineering, 13*(2), 191–206. https://doi.org/10.5101/nbe.v13i2.p191-206

52. Al Azzam, S., Ullah, Z., Azmi, S., Islam, M., Ahmad, I., & Hussain, M. K. (2024) . Tricyclic microwave-assisted synthesis of gold nanoparticles for biomedical applications: Combatting multidrug-resistant bacteria and fungus. *Beni-Suef University Journal of Basic and Applied Sciences, 13*(1), 53. https://doi.org/10.1186/s43088-024-00514-9

53. Nguyen, N. T. T., Nguyen, L. M., Nguyen, T. T. T., Nguyen, T. T., Nguyen, D. T. C., & Tran, T. V. (2022) . Formation, antimicrobial activity, and biomedical performance of plant-based nanoparticles: A review. *Environmental Chemistry Letters, 20*(4), 2531–2571. https://doi.org/10.1007/s10311-022-01425-w

54. Medda, S., Hajra, A., Dey, U., Bose, P., & Mondal, N. K. (2015) . Biosynthesis of silver nanoparticles from *Aloe vera* leaf extract and antifungal activity against *Rhizopus* sp. and *Aspergillus* sp. *Applied Nanoscience, 5*(7), 875–880. https://doi.org/10.1007/s13204-014-0387-1

55. Ahmad, N., Malik, M. A., Wani, A. H., & Bhat, M. Y. (2024) . Biogenic silver nanoparticles from fungal sources: Synthesis, characterization, and antifungal potential. *Microbial Pathogenesis, 193*, 106742. https://doi.org/10.1016/j.micpath.2024.106742

56. Piruthiviraj, P., Margret, A., & Krishnamurthy, P. P. (2016) . Gold nanoparticles synthesized by *Brassica oleracea* (Broccoli) acting as antimicrobial agents against human pathogenic bacteria and fungi. *Applied Nanoscience, 6*(4), 467–473. https://doi.org/10.1007/s13204-015-0460-4

57. Sami, A. (2019) . Antifungal effect of gold nanoparticles on fungi isolated from onychomycosis patients. *Al-Azhar Journal of Pharmaceutical Sciences, 60*(2), 26–42. https://doi.org/10.21608/ajps.2019.70234

58. Fathima, A. F., Mani, R. J., & Sakthipandi, K. (2021) . Antifungal activity of iron-gold and cobalt-gold co-doped ZnO nanoparticles. *Advanced Materials Letters, 12*(6), 21061636. https://doi.org/10.5185/amlett.2021.061636